Frontiers of Information Technology & Electronic Engineering
www.jzus.zju.edu.cn; engineering.cae.cn; www.springerlink.com
ISSN 2095-9184 (print); ISSN 2095-9230 (online)
E-mail: jzus@zju.edu.cn

Fixed-time constrained acceleration reconstruction scheme for robotic exoskeleton via neural networks*

Tao XUE[1], Zi-wei WANG[1], Tao ZHANG†‡[1], Ou BAI[2], Meng ZHANG[1,3], Bin HAN[4]

[1]*Department of Automation, Tsinghua University, Beijing 100084, China*

[2]*Department of Electrical and Computer Engineering, Florida International University, Miami 33174, USA*

[3]*Move Robotics Technology Co., Ltd., Shanghai 201306, China*

[4]*School of Mechanical Science and Engineering, Huazhong University of Science and Technology, Wuhan 430074, China*

†E-mail: taozhang@tsinghua.edu.cn

Received Aug. 21, 2019; Revision accepted Dec. 5, 2019; Crosschecked Apr. 7, 2020

Abstract: Accurate acceleration acquisition is a critical issue in the robotic exoskeleton system, but it is difficult to directly obtain the acceleration via the existing sensing systems. The existing algorithm-based acceleration acquisition methods put more attention on finite-time convergence and disturbance suppression but ignore the error constraint and initial state irrelevant techniques. To this end, a novel radical bias function neural network (RBFNN) based fixed-time reconstruction scheme with error constraints is designed to realize high-performance acceleration estimation. In this scheme, a novel exponential-type barrier Lyapunov function is proposed to handle the error constraints. It also provides a unified and concise Lyapunov stability-proof template for constrained and non-constrained systems. Moreover, a fractional power sliding mode control law is designed to realize fixed-time convergence, where the convergence time is irrelevant to initial states or external disturbance, and depends only on the chosen parameters. To further enhance observer robustness, an RBFNN with the adaptive weight matrix is proposed to approximate and attenuate the completely unknown disturbances. Numerical simulation and human subject experimental results validate the unique properties and practical robustness.

Key words: Acceleration reconstruction; Fixed-time convergence; Constrained control; Barrier Lyapunov function; Initial state irrelevant technique; Robotic exoskeleton

https://doi.org/10.1631/FITEE.1900418 **CLC number:** TP242

1 Introduction

Wearable exoskeleton is a powered anthropomorphic electromechanical system for strength enhancement, load carrying, exercise rehabilitation, and walking assistance (Xue et al., 2019). An increasing number of people show a strong need for the assistive robotic exoskeleton, e.g., walking assistance for elderly and disabled people with weakened skeletal muscles, load carrying for individual combat systems, and injury prevention for industrial workers (Xue et al., 2018). Regarding walking assistance, Kim J et al. (2018, 2019) developed an autonomous and portable hip soft exosuit to augment human walking and running, and experiments showed a reduced metabolic rate of walking by 9.3% and running by 4.0%. Seo et al. (2018) proposed a robotic lower-limb exoskeleton named GEMS-L to assist in walking and getting up. Chen Q et al. (2018) developed a dynamic balance gait control algorithm for spinal cord injury patients to stand and walk again. Zhang et al. (2019) proposed a unified admittance shaping

‡ Corresponding author

* Project supported by the Move Robotics Technology Co., Ltd. and the National Natural Science Foundation of China (No. 51705163)

ORCID: Tao XUE, https://orcid.org/0000-0001-7499-6160; Tao ZHANG, https://orcid.org/0000-0002-2980-6281

based assistive controller to reduce muscle activation and increase agility. To achieve the optimal assistive performance, Kang et al. (2019) explored the relationship between the assistance magnitude and the energetic cost benefits and found a U-shape trend metabolic cost. He Y et al. (2019) proposed a novel autonomous exoskeleton named Auto-LEE to maintain balance and provide walking assistance without extra support. As for the power amplification exoskeleton, Long et al. (2018) developed a hydraulically actuated exoskeleton, where an intention-driven control scheme was proposed to achieve human adaptive assistance. To improve the robustness of hydraulic actuation, Chen S et al. (2017) proposed a cascade force control strategy to address the nonlinear high-order dynamics and modeling uncertainties. Kim H et al. (2017) developed a hydraulic lower extremity exoskeleton and hybrid locomotion control algorithms to enhance mobility. In recent years, artificial muscle has attracted a lot of attention for its light weight, compactness, and high flexibility, and it has been successfully applied in various wearable equipment (Dong et al., 2018).

As a typical human-robot interaction system, collaborative control is particularly important for assisting as needed. In this category, both load-carrying control, such as sensitivity amplification control in BLEEX (Kazerooni et al., 2005; Zoss et al., 2006), and active impedance control (Aguirre-Ollinger et al., 2007), e.g., inertial, damping, and stiffness compensation or integral impedance shaping algorithms (Nagarajan et al., 2016), are heavily dependent on acceleration signals. Moreover, acceleration is directly correlated with the interaction force with Newton's second law and has the fastest response to interaction dynamics. Consequently, motion intention estimation, based on the acceleration observation, has been studied in Huo et al. (2016) and Kuo et al. (2018), where the voluntary muscle forces were evaluated via a complete kinetic model. As a result, acceleration is extremely essential in dynamical modeling, assistance planning, and motion intention estimation of exoskeleton systems. However, it cannot be directly measured from existing commonly applied sensors (e.g., encoders or optical measurement systems). Furthermore, due to the complex interaction disturbances and fast-changing acceleration signals, accurate acceleration estimation remains challenging.

Several methods have been investigated so far to obtain the ideal differential signal from limited measurements, and they can be roughly divided into two categories: model-free and model-based approaches. In the model-free scheme, the desired acceleration is directly calculated from the measurable velocity signal, where the state transition equations are not necessary. Direct difference from velocity is the most intuitive approach; however, it is quite sensitive to measurement noise, especially to non-differentiable noises. Acceleration reconstruction through a state observer is an alternative approach. The Luenberger state observer is a commonly applied differential observer, where the estimation errors are injected into the observer via linear feedback to ensure that the constructed acceleration will approach the true signal (Luenberger, 1966). In this case, the desired performance (e.g., convergence rate and noise suppression) is balanced by zero-pole placement. To further improve performance, an extended state observer was introduced into this scheme to attenuate the disturbance (Li et al., 2011). Higher observation accuracy is obtained because the convergence rate and noise suppression are decoupled. The above linear theory based observers guarantee only asymptotic convergence, which means that the observation errors will converge to zero as time goes to infinity. To obtain a higher convergence rate and better disturbance rejection performance, a finite-time observer such as Levant's arbitrary order sliding mode robust differentiator was proposed (Shtessel et al., 2014), but the Lyapunov stability and exact convergence time were not available. Regarding the kinetic model-based scheme, several acceleration reconstruction approaches have been developed. According to the cyclic feature of the quasi-cyclic signal in the exoskeleton system, a real-time delayless estimation of derivatives from noisy sensor signals was proposed (Tanghe et al., 2018), where the original and the derivative of the previous cycle were fed into a complementary fusion filter as the virtual measurement. In this approach, delayless acceleration was obtained by fusing prior virtual and current measurements. In the model-based finite-time observer category, a class of sliding mode observers for the nonlinear system have been first proposed to achieve finite-time convergence (Tan et al., 2010). Different from linear observers, a nonlinear discontinuous switching control was introduced to achieve finite-time convergence,

whereas traditional observers can guarantee only asymptotic convergence. In this framework, a robust finite-time velocity observer was proposed using homogeneous and Lyapunov theories, where the external disturbance on estimation precision can be suppressed to a relatively low level (He S and Lin, 2018). A full-order finite-time observer that uses only output position feedback has been designed to achieve finite-time tracking for robotic manipulators (Abooee et al., 2017). A neural network and a fast-integral terminal sliding mode based finite-time velocity observer were developed to achieve higher estimation precision, where the neural network was proposed to approximate and attenuate system uncertainties, while the remaining disturbance was handled with fast terminal sliding mode control (Yang Y et al., 2017). A fixed-time velocity reconstruction scheme with state constraints was proposed in Wang et al. (2019b), where full-state observation errors were guaranteed within the prescribed constraints. A sliding mode observer was developed to reconstruct the full states, where the reconstructed signal can approximate the true value to any accuracy in the presence of structural uncertainties and actuator faults (Xiao and Yin, 2016).

In summary, in the model-free scheme, the linear theory based observer can guarantee only asymptotic convergence, and the exact convergence time is not available in Levant's arbitrary order robust differentiator observer. In contrast, model-based methods have more potential for faster convergence and quantitative evaluation. However, the transient performance of observation errors and fixed-time convergence are still not guaranteed. In the above research, the convergence time is highly dependent on the initial states, and the observation error might appear to be largely an overshoot. Note that the initial states are difficult to obtain due to the uncertainty of the absolute attitude of the exoskeleton base, and the initial acceleration calculated by the joint angle often includes bias, which might result in distortion. Moreover, in the coupling system, the additional acceleration by the human interaction force is completely unmeasurable, which will lead to a sudden change of initial acceleration. As a consequence, the inaccurate states would definitely degrade the observer performance and even cause instability. In addition, the large overshoot on the acceleration estimation errors may result in a completely wrong control output, which will cause system damage or even threaten human safety. Thus, the maximum estimation errors must be limited in a reasonable region. These drawbacks seriously limit the practical applications of an acceleration observer. However, to the best knowledge of the authors, the initial state irrelevant and observation error constraint techniques in acceleration observation have not been well explored, which finally motivates this study.

To address these challenges, in this study we present an adaptive fixed-time acceleration reconstruction scheme with error constraints. The bases of this scheme are the design of the exponential-type barrier Lyapunov function (EBLF), the fractional power sliding mode control law, and radical bias function neural networks (RBFNNs), which are used to realize the error constraint, fixed-time convergence, and disturbance rejection, respectively. The main contributions are as follows:

1. We present a new EBLF to address the error constraint issues and reveal the equivalence between EBLF and the commonly used quadratic function when there are no constraints. Different from the log-type barrier Lyapunov function, EBLF is a more general Lyapunov function that can also be applied in a non-constraint system. Moreover, EBLF provides an alternative barrier Lyapunov function design template, where the stability proof is more concise.

2. An acceleration reconstruction scheme is developed to achieve high-performance observation. Other methods can realize only disturbance suppression and finite-time convergence, whereas this study presents a more general solution to address another two practical application problems. The convergence time is irrelevant to the initial states or disturbance, and dependent on only the chosen parameters. Moreover, the observation errors are strictly limited within the prescribed error bounds.

3. The proposed scheme provides high-precision acceleration estimation in an actual exoskeleton system, which will contribute to developing better acceleration-dependent control algorithms. Moreover, fixed-time convergence and initial state irrelevance techniques enhance the practicality of the reconstruction algorithm, where no prior knowledge is required in the form of perturbation or the initial states. Furthermore, the error constraint provides a specific quantitative index for the design of a safe robotic exoskeleton controller.

2 Problem formulation and preliminaries

The problem is to let the reconstructed signal track actual acceleration as accurately as possible in the shortest time while maintaining internal stability. To be more specific, in the presence of interaction disturbance and system uncertainties, an acceleration reconstruction scheme is designed such that (1) the acceleration reconstruction errors never exceed the prescribed constraints and (2) the observation errors are guaranteed to converge in a fixed time, which is completely independent of the initial states and disturbances.

2.1 Exoskeleton platform

We have developed a powered hip assistive exoskeleton (Fig. 1), which is composed of a hybrid soft-rigid waist belt, a backpack with power supply, driver boards and control modules, and two series elastic actuators (SEA) connected with two links down to the thigh. The exoskeleton has four degrees of freedom (DOF) aligned with the hip, where two active joints are in the flexion-extension direction to provide active assistance, while the other two passives are in the adduction-abduction direction for walking agility. It can be seen that the actuation system and joint DOF configuration of exoskeletons are the same as those of traditional robots; thus, the kinetic model can be formed with traditional Newton-Euler or Lagrange methods. The essential characteristic of the robotic exoskeleton is the human-in-the-loop model, where the exoskeleton dynamics can not only be affected by internal disturbances from the driving system but also strongly disturbed by unpredictable ever-changing body movements.

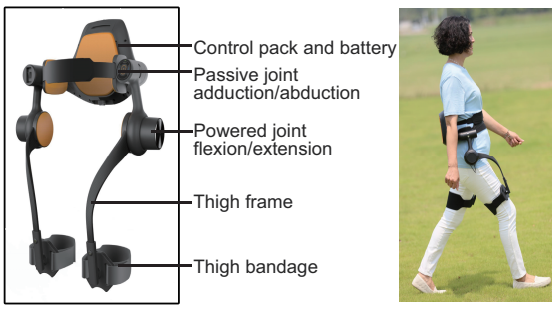

Fig. 1 Prototype of the developed hip assistive exoskeleton

2.2 Exoskeleton dynamics

Consider an n-DOF robotic exoskeleton system, in which the kinetic model can be expressed as

$$\boldsymbol{H}(\boldsymbol{q})\ddot{\boldsymbol{q}}+\boldsymbol{C}(\boldsymbol{q},\dot{\boldsymbol{q}})\dot{\boldsymbol{q}}+\boldsymbol{G}(\boldsymbol{q})=\bar{\boldsymbol{\tau}}+\bar{\boldsymbol{\delta}}(\boldsymbol{q},\dot{\boldsymbol{q}}), \quad (1)$$

where $\boldsymbol{q}\in\mathbb{R}^{n\times 1}$, $\dot{\boldsymbol{q}}\in\mathbb{R}^{n\times 1}$, and $\ddot{\boldsymbol{q}}\in\mathbb{R}^{n\times 1}$ represent the vectors of joint positions, velocities, and accelerations, respectively. $\boldsymbol{H}(\boldsymbol{q})\in\mathbb{R}^{n\times n}$ is the positive-definite inertial matrix, while $\boldsymbol{C}(\boldsymbol{q},\dot{\boldsymbol{q}})\in\mathbb{R}^{n\times n}$ denotes the Coriolis and centrifugal matrix. $\boldsymbol{G}(\boldsymbol{q})\in\mathbb{R}^{n\times 1}$ stands for the gravity term and $\bar{\boldsymbol{\tau}}\in\mathbb{R}^{n\times 1}$ is the force applied to the exoskeleton joints. $\bar{\boldsymbol{\delta}}(\boldsymbol{q},\dot{\boldsymbol{q}})$ represents the unknown lumped disturbance, which consists of external disturbance, internal disturbance, and modeling uncertainties. $\bar{\boldsymbol{\tau}}$ and $\bar{\boldsymbol{\delta}}$ are assumed to be continuous. If we take the first derivative of both sides of Eq. (1), we have

$$\dot{\boldsymbol{H}}\dot{\boldsymbol{q}}+\boldsymbol{H}\ddot{\boldsymbol{q}}+\dot{\boldsymbol{C}}\dot{\boldsymbol{q}}+\boldsymbol{C}\ddot{\boldsymbol{q}}+\dot{\boldsymbol{G}}=\boldsymbol{\tau}+\boldsymbol{\delta}, \quad (2)$$

where $\boldsymbol{\tau}$ and $\boldsymbol{\delta}$ are the time derivatives of $\bar{\boldsymbol{\tau}}$ and $\bar{\boldsymbol{\delta}}$, respectively. The disturbance $\boldsymbol{\delta}$ is assumed to be continuous and depends only on the velocity and acceleration. A similar assumption was made in Wang et al. (2019a).

2.3 Preliminaries

Property 1 $\boldsymbol{H}$ is uniformly symmetric positive-definite with lower and upper bounds (Yang ZY et al., 2017):

$$0<\underline{\lambda}_{\mathrm{H}}\boldsymbol{I}<\boldsymbol{H}(\boldsymbol{q})<\bar{\lambda}_{\mathrm{H}}\boldsymbol{I}<+\infty. \quad (3)$$

Property 2 $\dot{\boldsymbol{H}}+\boldsymbol{C}$ is uniformly positive-definite and there exist positive upper and lower bounds such that

$$0<\underline{\lambda}_{\mathrm{HC}}\boldsymbol{I}<\dot{\boldsymbol{H}}(\boldsymbol{q},\dot{\boldsymbol{q}})<\bar{\lambda}_{\mathrm{HC}}\boldsymbol{I}<+\infty. \quad (4)$$

Property 3 Similar to Wang et al. (2018), we assume that the nonlinear function $\dot{\boldsymbol{C}}(\dot{\boldsymbol{q}},\ddot{\boldsymbol{q}})\dot{\boldsymbol{q}}$ is Lipschitz and there exists a positive scalar c such that

$$\|\dot{\boldsymbol{C}}(\dot{\boldsymbol{q}},\hat{\ddot{\boldsymbol{q}}})-\boldsymbol{C}(\dot{\boldsymbol{q}},\ddot{\boldsymbol{q}})\|\leq c\|\hat{\ddot{\boldsymbol{q}}}-\ddot{\boldsymbol{q}}\|, \quad (5)$$

where $\hat{\ddot{\boldsymbol{q}}}$ denotes the estimate of the vector of joint accelerations.

Lemma 1 Consider the following differential system (Polyakov, 2011; Zhu et al., 2011):

$$\dot{\boldsymbol{x}}=f(\boldsymbol{x}),\quad \boldsymbol{x}(0)\in\mathbb{R}^{n\times 1},\quad \boldsymbol{x}\in\boldsymbol{U}\backslash\{\boldsymbol{0}\}, \quad (6)$$

where $\boldsymbol{U}$ denotes the whole vector set of real numbers.

Suppose that there exists a positive continuous-differential function $V(\boldsymbol{x}):\boldsymbol{U}\to\mathbb{R}_+$ such that

$$\dot{V}(\boldsymbol{x})\le-(\alpha V^p(\boldsymbol{x})+\beta V^q(\boldsymbol{x}))^k+\phi,$$

where $\alpha,\beta,\phi>0$, $0<pk<1$, $qk>1$. Then the system is fixed-time stable. The settling time T and convergence region D can be obtained as

$$\begin{cases}T\le\dfrac{1}{\alpha^k\zeta^k(1-pk)}+\dfrac{1}{\beta^k\zeta^k(qk-1)},\\ D=\{\lim\limits_{t\to T}\boldsymbol{x}|V(\boldsymbol{x})<M\},\\ M=\min\left(\alpha^{-\frac{1}{p}}\left(\dfrac{\phi}{1-\zeta^k}\right)^{\frac{1}{kp}},\beta^{-\frac{1}{q}}\left(\dfrac{\phi}{1-\zeta^k}\right)^{\frac{1}{kq}}\right),\end{cases}\tag{7}$$

where ζ is a positive scalar, $0<\zeta\le1$.

Remark 1 It can be seen from Eq. (7) that the settling time has no initial state terms, indicating that the system is fixed-time stable and independent of the initial states. Moreover, because D is directly related to α and β, the convergence region can be arbitrarily small with properly selected parameters.

Lemma 2 The following inequality holds with $a_1,a_2,\ldots,a_n\ge0$ and $c>0$:

$$(a_1+a_2+\ldots+a_n)^c\le\max(n^{c-1},1)\cdot(a_1^c+a_2^c+\ldots+a_n^c).\tag{8}$$

Lemma 3 The inequality $(|x_1|+|x_2|+\ldots+|x_n|)^p\le|x_1|^p+|x_2|^p+\ldots+|x_n|^p$ holds for $x_i\in\mathbb{R}$, where p is a real number satisfying $0<p\le1$.

Lemma 4 With the universal approximation property of neural networks (NNs), there exists an NN for any continuous function $\boldsymbol{f}(\boldsymbol{X})$ such that (Fei and Ding, 2012; Hua et al., 2013)

$$\boldsymbol{f}(\boldsymbol{X})=(\boldsymbol{W}^*)^{\mathrm{T}}\boldsymbol{\varphi}(\boldsymbol{X})+\boldsymbol{\epsilon}^*,\quad||\boldsymbol{\epsilon}^*||\le\epsilon_N,\tag{9}$$

where $\boldsymbol{\varphi}(\boldsymbol{X})$ is the RBF vector function, $\boldsymbol{W}^*$ denotes the optimal weight matrix, $\boldsymbol{\epsilon}^*$ represents the approximation error, and ϵ_N is the upper bound of $\boldsymbol{\epsilon}^*$.

2.4 Exponential-type barrier Lyapunov function

A novel EBLF is designed as

$$\Psi(l,\boldsymbol{z})=l^2\left(\exp\frac{\boldsymbol{z}^{\mathrm{T}}\boldsymbol{z}}{l^2-\boldsymbol{z}^{\mathrm{T}}\boldsymbol{z}}-1\right),\tag{10}$$

where $\boldsymbol{z}=[z_1,z_2,\ldots,z_n]^{\mathrm{T}}$ denotes the state variables to be constrained and $l(t)\in\mathbb{R}_+$ is the predefined continuous-differentiable constraint function (abbreviated as l in this study). The proposed EBLF has the following properties:

1. Suppose the state variables are bounded with the predefined constraint. With $\mathrm{e}^x-1\ge x$ and $x\ge0$, one has

$$\Psi(l,\boldsymbol{z})\ge l^2\frac{\boldsymbol{z}^{\mathrm{T}}\boldsymbol{z}}{l^2-\boldsymbol{z}^{\mathrm{T}}\boldsymbol{z}}\ge0,\tag{11}$$

which implies that the designed function is positive when the state belongs to the set $\{\boldsymbol{z}|\|\boldsymbol{z}\|\le l,\boldsymbol{z}\in\boldsymbol{U}\backslash\{\boldsymbol{0}\}\}$.

2. The proposed EBLF will approach infinity when the state variables get close to the predefined boundary:

$$\lim_{||\boldsymbol{z}||\to l}\Psi(l,\boldsymbol{z})=+\infty.\tag{12}$$

3. When there is no constraint on the state variable $\boldsymbol{z}$, i.e., $l\to\infty$, EBLF has the form by using L'Hopital's rule:

$$\lim_{l\to\infty}\Psi(l,\boldsymbol{z})=\boldsymbol{z}^{\mathrm{T}}\boldsymbol{z}.\tag{13}$$

Remark 2 It can be seen that EBLF will degrade into a quadratic term when $l\to\infty$, which implies that it is still an applicable Lyapunov function when there is no constraint. Because the traditional log-type barrier Lyapunov function will approach infinity when $l\to\infty$, it can be applied only in the constrained situation.

3 Acceleration reconstruction scheme design

The schematic of the proposed NN-based fixed-time acceleration reconstruction scheme is presented in Fig. 2. To obtain an ideal acceleration estimate, the fractional power sliding mode control law is first designed to achieve fixed-time convergence, where the feedback gains are tuned to guarantee constrained observation errors. Regarding the disturbances, an RBFNN with the adaptive weight matrix law is further proposed to approximate and attenuate most disturbances, while the remaining perturbation is left to the sliding mode control law to suppress. The detailed explanations are as follows.

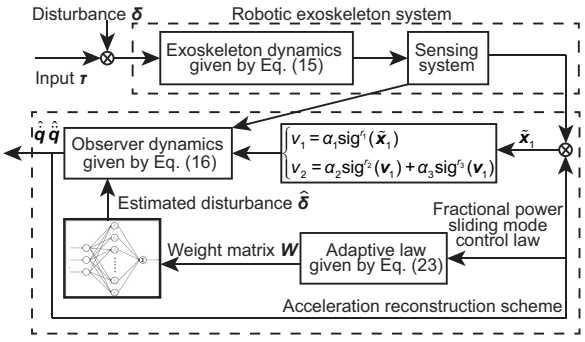

Fig. 2 Schematic of the proposed fixed-time acceleration reconstruction scheme

3.1 Coordination transformation

First, let $\boldsymbol{x}_1 = \dot{\boldsymbol{q}}$ and $\bar{\boldsymbol{x}}_2 = \ddot{\boldsymbol{q}}$. Then the dynamical model of robotic exoskeleton can be rewritten as

$$\begin{cases} \dot{\boldsymbol{x}}_1 = \bar{\boldsymbol{x}}_2, \\ \dot{\bar{\boldsymbol{x}}}_2 = -\boldsymbol{H}^{-1}\dot{\boldsymbol{H}}\ddot{\boldsymbol{q}} - \boldsymbol{H}^{-1}\dot{\boldsymbol{C}}\dot{\boldsymbol{q}} - \boldsymbol{H}^{-1}\boldsymbol{C}\ddot{\boldsymbol{q}} \\ \qquad\quad - \boldsymbol{H}^{-1}\dot{\boldsymbol{G}} + \boldsymbol{H}^{-1}\boldsymbol{\tau} + \boldsymbol{H}^{-1}\boldsymbol{\delta}. \end{cases} \tag{14}$$

Let $\boldsymbol{x}_2 = \bar{\boldsymbol{x}}_2 - \boldsymbol{T}\boldsymbol{x}_1$, where $\boldsymbol{T}$ is the positive-definite coordination transformation matrix. Then Eq. (14) has the form

$$\begin{cases} \dot{\boldsymbol{x}}_1 = \boldsymbol{x}_2 + \boldsymbol{T}\boldsymbol{x}_1, \\ \dot{\boldsymbol{x}}_2 = -\boldsymbol{H}^{-1}\dot{\boldsymbol{H}}\ddot{\boldsymbol{q}} - \boldsymbol{H}^{-1}\dot{\boldsymbol{C}}\dot{\boldsymbol{q}} - \boldsymbol{H}^{-1}\boldsymbol{C}\ddot{\boldsymbol{q}} \\ \qquad\quad - \boldsymbol{H}^{-1}\dot{\boldsymbol{G}} + \boldsymbol{H}^{-1}\boldsymbol{\tau} + \boldsymbol{H}^{-1}\boldsymbol{\delta} - \boldsymbol{T}^2\boldsymbol{x}_1 - \boldsymbol{T}\boldsymbol{x}_2. \end{cases} \tag{15}$$

Remark 3 In linear differential equations, the coefficient matrix governs the performance and stability of the system. With the added transformation term $\boldsymbol{T}$, we have more selectable control variables in the governing matrix, which leaves more degrees for controller design.

3.2 Finite-time acceleration observer design

The acceleration observer is designed as

$$\begin{cases} \dot{\hat{\boldsymbol{x}}}_1 = \hat{\boldsymbol{x}}_2 + \boldsymbol{T}\hat{\boldsymbol{x}}_1 - \boldsymbol{K}_1\tilde{\boldsymbol{x}}_1 - \boldsymbol{v}_1, \\ \dot{\hat{\boldsymbol{x}}}_2 = -\boldsymbol{H}^{-1}(\dot{\boldsymbol{H}} + \boldsymbol{C})\hat{\dot{\boldsymbol{q}}} - \boldsymbol{H}^{-1}\dot{\boldsymbol{C}}\dot{\boldsymbol{q}} \\ \qquad\quad - \boldsymbol{H}^{-1}(\dot{\boldsymbol{G}} - \dot{\boldsymbol{\tau}}) + \boldsymbol{H}^{-1}\boldsymbol{\delta}(\dot{\boldsymbol{q}}, \hat{\dot{\boldsymbol{q}}}) - \boldsymbol{T}^2\hat{\boldsymbol{x}}_1 \\ \qquad\quad - \boldsymbol{T}\hat{\boldsymbol{x}}_2 - \boldsymbol{K}_2\tilde{\boldsymbol{x}}_1 - \boldsymbol{v}_2 - \alpha_4\mathrm{sign}(\tilde{\boldsymbol{x}}_1), \\ \mathrm{sig}(\boldsymbol{\xi})^\alpha = \Big[|\xi_1|^\alpha\mathrm{sign}(\xi_1), |\xi_2|^\alpha\mathrm{sign}(\xi_2), \ldots, \\ \qquad\quad |\xi_n|^\alpha\mathrm{sign}(\xi_n)\Big], \\ \boldsymbol{\xi} = [\xi_1, \xi_2, \ldots, \xi_n]^{\mathrm{T}}, \end{cases} \tag{16}$$

where $\boldsymbol{v}_1 = \alpha_1\mathrm{sig}^{r_1}(\tilde{\boldsymbol{x}}_1)$, $\boldsymbol{v}_2 = \alpha_2\mathrm{sig}^{r_2}(\boldsymbol{v}_1) + \alpha_3\mathrm{sig}^{r_3}(\boldsymbol{v}_1)$, and $\alpha_i > 0$ $(i = 1, 2, 3, 4)$ are the feedback gains. $r_1 > 1$, $r_2 > 0$, and $r_3 > 0$ satisfy the following inequalities $0 < r_1 r_2 < 1$ and $r_1 r_3 > 1$. $\hat{\boldsymbol{x}}_1, \hat{\boldsymbol{x}}_2$, and $\hat{\dot{\boldsymbol{q}}}$ are the estimates of $\boldsymbol{x}_1, \boldsymbol{x}_2$, and $\dot{\boldsymbol{q}}$, respectively. $\boldsymbol{K}_1 = \mathrm{diag}(k_{11}, k_{12}, \ldots, k_{1n})$ and $\boldsymbol{K}_2 = \mathrm{diag}(k_{21}, k_{22}, \ldots, k_{2n})$ are positive-definite diagonal matrices such that $\boldsymbol{A}$ is Hurwitz.

$$\boldsymbol{A} = \begin{bmatrix} \boldsymbol{T} - \boldsymbol{K}_1 & \boldsymbol{I} \\ -(\boldsymbol{T}^2 + \boldsymbol{K}_2) & -\boldsymbol{T} \end{bmatrix}. \tag{17}$$

Combining Eq. (16) with Eq. (15), the error dynamics can be obtained as

$$\begin{cases} \dot{\tilde{\boldsymbol{x}}}_1 = (\boldsymbol{T} - \boldsymbol{K}_1)\tilde{\boldsymbol{x}}_1 + \tilde{\boldsymbol{x}}_2 - \boldsymbol{v}_1, \\ \dot{\tilde{\boldsymbol{x}}}_2 = -(\boldsymbol{T}^2 + \boldsymbol{K}_2)\tilde{\boldsymbol{x}}_1 - \boldsymbol{T}\tilde{\boldsymbol{x}}_2 \\ \qquad\quad - \boldsymbol{H}^{-1}(\dot{\boldsymbol{H}} + \boldsymbol{C})(\hat{\dot{\boldsymbol{q}}} - \ddot{\boldsymbol{q}}) - \boldsymbol{H}^{-1}(\hat{\dot{\boldsymbol{C}}} - \dot{\boldsymbol{C}})\dot{\boldsymbol{q}} \\ \qquad\quad + (\hat{\boldsymbol{Q}} - \boldsymbol{Q}) - \boldsymbol{v}_2 - \alpha_4\mathrm{sign}(\tilde{\boldsymbol{x}}_1), \end{cases} \tag{18}$$

where $\hat{\boldsymbol{Q}} = \boldsymbol{H}^{-1}\hat{\boldsymbol{\delta}}$ and $\boldsymbol{Q} = \boldsymbol{H}^{-1}\boldsymbol{\delta}$. Joint position $\boldsymbol{q}$ and velocity $\dot{\boldsymbol{q}}$ are available in this study, and the disturbance term $\boldsymbol{Q}$ is approximated with RBFNNs,

$$\widehat{\boldsymbol{Q}} = \widehat{\boldsymbol{W}}^{\mathrm{T}}\boldsymbol{\varphi}(\dot{\boldsymbol{q}}, \hat{\dot{\boldsymbol{q}}}). \tag{19}$$

With Lemma 4, the approximation error can be further derived:

$$\begin{cases} \widetilde{\boldsymbol{Q}} = \widetilde{\boldsymbol{W}}\boldsymbol{\varphi}(\dot{\boldsymbol{q}}, \hat{\dot{\boldsymbol{q}}}) + \boldsymbol{N} - \boldsymbol{\epsilon}^*, \\ \widetilde{\boldsymbol{Q}} = \widehat{\boldsymbol{Q}} - \boldsymbol{Q}, \\ \boldsymbol{N} = (\boldsymbol{W}^*)^{\mathrm{T}}\boldsymbol{\varphi}(\dot{\boldsymbol{q}}, \hat{\dot{\boldsymbol{q}}}) - (\boldsymbol{W}^*)^{\mathrm{T}}\boldsymbol{\varphi}(\dot{\boldsymbol{q}}, \ddot{\boldsymbol{q}}), \\ \widetilde{\boldsymbol{W}} = \widehat{\boldsymbol{W}} - \boldsymbol{W}. \end{cases} \tag{20}$$

Define new matrices as

$$\begin{cases} \boldsymbol{\Phi} = \begin{bmatrix} \boldsymbol{0} \\ -\boldsymbol{H}^{-1}(\dot{\boldsymbol{H}} + \boldsymbol{C})(\hat{\dot{\boldsymbol{q}}} - \ddot{\boldsymbol{q}}) - \boldsymbol{H}^{-1}(\hat{\dot{\boldsymbol{C}}} - \dot{\boldsymbol{C}})\dot{\boldsymbol{q}} \end{bmatrix}, \\ \boldsymbol{\Gamma} = \begin{bmatrix} \boldsymbol{0} \\ \widehat{\boldsymbol{Q}} - \boldsymbol{Q} \end{bmatrix}, \\ \boldsymbol{\Lambda} = \begin{bmatrix} -\boldsymbol{v}_1 \\ -\boldsymbol{v}_2 - \alpha_4\mathrm{sign}(\tilde{\boldsymbol{x}}_1) \end{bmatrix}. \end{cases} \tag{21}$$

Then, the error dynamics can be further simplified as

$$\dot{\tilde{\boldsymbol{x}}} = \boldsymbol{A}\tilde{\boldsymbol{x}} + \boldsymbol{\Phi} + \boldsymbol{\Gamma} + \boldsymbol{\Lambda}. \tag{22}$$

Theorem 1 For the acceleration observer error system (16), choose the adaptive parameter laws for

RBFNNs as

$$\begin{cases}\widehat{\boldsymbol{W}}=\dfrac{l_b^2}{l_b^2-R_1^2}\mathrm{e}^{\frac{R_1^2}{l_b^2-R_1^2}}(\boldsymbol{\eta}\boldsymbol{\varphi}(\dot{\boldsymbol{q}},\hat{\dot{\boldsymbol{q}}})\dot{\boldsymbol{q}}^{\mathrm{T}}-\boldsymbol{\eta}\boldsymbol{\pi}),\\ \dot{\boldsymbol{\pi}}=\dfrac{\mathrm{d}\boldsymbol{\varphi}\left(\dot{\boldsymbol{q}},\hat{\dot{\boldsymbol{q}}}\right)}{\mathrm{d}t}\dot{\boldsymbol{q}}^{\mathrm{T}}+\boldsymbol{\varphi}(\dot{\boldsymbol{q}},\hat{\dot{\boldsymbol{q}}})(\hat{\boldsymbol{x}}_2+\boldsymbol{T}\dot{\boldsymbol{q}})^{\mathrm{T}},\end{cases}\tag{23}$$

where $\boldsymbol{\eta}\in\mathbb{R}^{q\times n}$ is a positive-definite diagonal filter coefficient matrix, l_b is the upper bound of $\tilde{\boldsymbol{x}}_2$, and R_1 is the radius of the attraction region for observation errors. If the following conditions hold:

$$\begin{cases}\boldsymbol{P}\boldsymbol{A}+\boldsymbol{A}^{\mathrm{T}}\boldsymbol{P}+\dfrac{\varepsilon_1\varepsilon_2}{\varepsilon_1+\varepsilon_2}\boldsymbol{P}\boldsymbol{P}<\boldsymbol{0},\\ -\lambda_{\max}\left(\boldsymbol{T}+\boldsymbol{H}^{-1}(\dot{\boldsymbol{H}}+\boldsymbol{C})-\dfrac{1}{\varepsilon_2}\boldsymbol{I}\right)-\dfrac{1}{\underline{\lambda}_{\mathrm{H}}}-\varepsilon_2 b^2>0,\\ -\lambda_{\max}(\boldsymbol{T}-\boldsymbol{K}_1)\geq\dfrac{c_7l_a^2+c_{10}\|\tilde{\boldsymbol{x}}_1\|^2}{\|\tilde{\boldsymbol{x}}_1\|^2+\varepsilon_0},\\ \alpha_1\geq R_1,\\ \alpha_2\geq\dfrac{c_{14}l_b^2+c_{15}\|\tilde{\boldsymbol{x}}_2\|^{r_2+1}}{\|\tilde{\boldsymbol{x}}_2\|^{r_2+1}+\varepsilon_0},\\ \alpha_4\geq\epsilon_N,\end{cases}\tag{24}$$

the acceleration estimation error will converge in fixed time with the prescribed constraints. The definitions of $\boldsymbol{P}$, ε_0, ε_1, ε_2, c_7, c_{10}, c_{14}, c_{15}, l_a, and b will be discussed in Section 4.

4 Stability analysis

The proof of finite-time stability is divided into three steps. First, a traditional quadratic-type Lyapunov function is chosen to prove that the error will converge into a rough domain asymptotically. Then, with the results of step 1, EBLF is constructed to demonstrate the fixed-time stability of $\tilde{\boldsymbol{x}}_1$. Based on the results of steps 1 and 2, EBLF is again used in step 3 to address the convergence performance (e.g., fixed-time convergence, initial state irrelevance, and prescribed error constraints) of acceleration reconstruction errors $\tilde{\boldsymbol{x}}_2$.

Step 1: Choose the candidate Lyapunov function as

$$V_1=\tilde{\boldsymbol{x}}^{\mathrm{T}}\boldsymbol{P}\tilde{\boldsymbol{x}}+\mathrm{tr}(\widetilde{\boldsymbol{W}}\boldsymbol{P}_2\widetilde{\boldsymbol{W}}^{\mathrm{T}}(\boldsymbol{\eta}^{\mathrm{T}})^{-1}),\tag{25}$$

where tr() represents the trace of a given matrix, $\boldsymbol{P}=\mathrm{diag}(\boldsymbol{P}_1,\boldsymbol{P}_2)$, $\boldsymbol{P}_1=\mathrm{diag}(p_{11},p_{12},\ldots,p_{1n})$, and $\boldsymbol{P}_2=\mathrm{diag}(p_{21},p_{22},\ldots,p_{2n})$. Differentiating V_1 with respect to time gives

$$\begin{aligned}\dot{V}_1=&\tilde{\boldsymbol{x}}^{\mathrm{T}}(\boldsymbol{P}\boldsymbol{A}+\boldsymbol{A}^{\mathrm{T}}\boldsymbol{P})\tilde{\boldsymbol{x}}+2\tilde{\boldsymbol{x}}^{\mathrm{T}}\boldsymbol{P}\boldsymbol{\Phi}+2\tilde{\boldsymbol{x}}^{\mathrm{T}}\boldsymbol{P}\boldsymbol{\Gamma}\\&+2\tilde{\boldsymbol{x}}^{\mathrm{T}}\boldsymbol{P}\boldsymbol{\Lambda}+2\mathrm{tr}\left(\widetilde{\boldsymbol{W}}\boldsymbol{P}_2\dot{\widetilde{\boldsymbol{W}}}^{\mathrm{T}}(\boldsymbol{\eta}^{\mathrm{T}})^{-1}\right).\end{aligned}\tag{26}$$

With the Young inequality, one has

$$\begin{aligned}&2\tilde{\boldsymbol{x}}^{\mathrm{T}}\boldsymbol{P}\boldsymbol{\Phi}\\\leq&\frac{1}{\varepsilon_1}\tilde{\boldsymbol{x}}^{\mathrm{T}}\boldsymbol{P}^2\tilde{\boldsymbol{x}}+\varepsilon_1\boldsymbol{\Phi}^{\mathrm{T}}\boldsymbol{\Phi}\\\leq&\frac{1}{\varepsilon_1}\tilde{\boldsymbol{x}}^{\mathrm{T}}\boldsymbol{P}^2\tilde{\boldsymbol{x}}+\varepsilon_1\left\|\boldsymbol{H}^{-1}(\dot{\boldsymbol{H}}+\boldsymbol{C})(\hat{\dot{\boldsymbol{q}}}-\ddot{\boldsymbol{q}})\right.\\&\left.-\boldsymbol{H}^{-1}(\hat{\dot{\boldsymbol{C}}}-\dot{\boldsymbol{C}})\dot{\boldsymbol{q}}\right\|^2,\end{aligned}\tag{27}$$

where ε_1 is a positive scalar. It can be further scaled as follows with Properties 1–3:

$$\begin{aligned}&2\tilde{\boldsymbol{x}}^{\mathrm{T}}\boldsymbol{P}\boldsymbol{\Phi}\\\leq&\frac{1}{\varepsilon_1}\tilde{\boldsymbol{x}}^{\mathrm{T}}\boldsymbol{P}^2\tilde{\boldsymbol{x}}+\varepsilon_1\frac{\bar{\lambda}_{\mathrm{HC}}^2}{\underline{\lambda}_{\mathrm{H}}^2}||\tilde{\boldsymbol{x}}_2+\boldsymbol{T}\tilde{\boldsymbol{x}}_1||^2\\&+\varepsilon_1\frac{c^2}{\underline{\lambda}_{\mathrm{H}}^2}||\tilde{\boldsymbol{x}}_2+\boldsymbol{T}\tilde{\boldsymbol{x}}_1||^2+2\varepsilon_1c\frac{\bar{\lambda}_{\mathrm{HC}}}{\underline{\lambda}_{\mathrm{H}}^2}||\tilde{\boldsymbol{x}}_2+\boldsymbol{T}\tilde{\boldsymbol{x}}_1||^2\\\leq&\frac{1}{\varepsilon_1}\tilde{\boldsymbol{x}}^{\mathrm{T}}\boldsymbol{P}^2\tilde{\boldsymbol{x}}+c_1||\tilde{\boldsymbol{x}}||^2,\end{aligned}\tag{28}$$

where $c_1=\varepsilon_1\dfrac{(\bar{\lambda}_{\mathrm{HC}}+c)^2}{\underline{\lambda}_{\mathrm{H}}^2}(\lambda_{\max}(\boldsymbol{T})+1)^2$. According to Lemma 4, it can be easily found that there exists a positive scalar b such that

$$\begin{aligned}||\boldsymbol{N}||=&\left\|(\boldsymbol{W}^*)^{\mathrm{T}}\boldsymbol{\varphi}\left(\dot{\boldsymbol{q}},\hat{\dot{\boldsymbol{q}}}\right)-(\boldsymbol{W}^*)^{\mathrm{T}}\boldsymbol{\varphi}\left(\dot{\boldsymbol{q}},\ddot{\boldsymbol{q}}\right)\right\|\\\leq&b||\hat{\dot{\boldsymbol{q}}}-\ddot{\boldsymbol{q}}||\leq b||\tilde{\boldsymbol{x}}_2+\boldsymbol{T}\tilde{\boldsymbol{x}}_1||.\end{aligned}\tag{29}$$

The above inequality leads to

$$\begin{aligned}&2\tilde{\boldsymbol{x}}^{\mathrm{T}}\boldsymbol{P}\boldsymbol{\Gamma}=2\tilde{\boldsymbol{x}}_2\boldsymbol{P}_2\left(\widetilde{\boldsymbol{W}}^{\mathrm{T}}\boldsymbol{\varphi}\left(\dot{\boldsymbol{q}},\hat{\dot{\boldsymbol{q}}}\right)+\boldsymbol{N}-\boldsymbol{\epsilon}^*\right)\\\leq&2\tilde{\boldsymbol{x}}_2^{\mathrm{T}}\boldsymbol{P}_2\widetilde{\boldsymbol{W}}^{\mathrm{T}}\boldsymbol{\varphi}\left(\dot{\boldsymbol{q}},\hat{\dot{\boldsymbol{q}}}\right)+\frac{1}{\varepsilon_2}\tilde{\boldsymbol{x}}^{\mathrm{T}}\boldsymbol{P}_2^2\tilde{\boldsymbol{x}}\\&+c_2||\tilde{\boldsymbol{x}}||^2+c_3||\tilde{\boldsymbol{x}}||,\end{aligned}\tag{30}$$

where $c_2=\varepsilon_2b^2\left(\lambda_{\max}\left(\boldsymbol{T}\right)+1\right)^2$, $c_3=2\lambda_{\max}(\boldsymbol{P}_2)\epsilon_N$, and ε_2 is a positive scalar. Note that the control term can be scaled as

$$\begin{aligned}&2\tilde{\boldsymbol{x}}^{\mathrm{T}}\boldsymbol{P}\boldsymbol{\Lambda}=-2\tilde{\boldsymbol{x}}^{\mathrm{T}}\boldsymbol{P}\begin{bmatrix}\boldsymbol{v}_1\\\boldsymbol{v}_2+\alpha_4\mathrm{sign}\left(\tilde{\boldsymbol{x}}_1\right)\end{bmatrix}\\&\leq2\left(\|\tilde{\boldsymbol{x}}_1^{\mathrm{T}}\boldsymbol{P}_1\boldsymbol{v}_1\|+\|\tilde{\boldsymbol{x}}_2^{\mathrm{T}}\boldsymbol{P}_2\boldsymbol{v}_2\|+\alpha_4\|\tilde{\boldsymbol{x}}_2^{\mathrm{T}}\boldsymbol{P}_2\mathrm{sign}\left(\tilde{\boldsymbol{x}}_1\right)\|\right)\\&\leq c_4||\tilde{\boldsymbol{x}}||,\end{aligned}\tag{31}$$

where $c_4 = \sum_{i=1}^{n}\Big(\alpha_1 p_{1i}\sqrt{|\tilde{x}_{1i}|^{2r_1}} + \alpha_2\alpha_1^{r_2}p_{2i}\cdot\sqrt{|\tilde{x}_{1i}|^{2r_1r_2}} + \alpha_3\alpha_1^{r_3}p_{2i}\sqrt{|\tilde{x}_{1i}|^{2r_1r_3}} + \alpha_4\sum_{i=1}^{n}p_{2i}\Big)$.

With the adaptive law (23) for the weight matrix of RBFNNs, it can be obtained that

$$\begin{aligned}&2\mathrm{tr}\left(\widetilde{\boldsymbol{W}}\boldsymbol{P}_2\dot{\widetilde{\boldsymbol{W}}}^{\mathrm{T}}(\boldsymbol{\eta}^{\mathrm{T}})^{-1}\right) = 2\mathrm{tr}\left(\widetilde{\boldsymbol{W}}\boldsymbol{P}_2\dot{\widehat{\boldsymbol{W}}}^{\mathrm{T}}\right)\\ &\le -2\tilde{\boldsymbol{x}}_2^{\mathrm{T}}\boldsymbol{P}_2\widetilde{\boldsymbol{W}}^{\mathrm{T}}\boldsymbol{\varphi}(\dot{\boldsymbol{q}},\hat{\dot{\boldsymbol{q}}}).\end{aligned}\tag{32}$$

Substituting inequalities (28) and (30)–(32) into Eq. (26), one has

$$\begin{aligned}\dot{V}_1 \le&\tilde{\boldsymbol{x}}^{\mathrm{T}}\left(\boldsymbol{P}\boldsymbol{A}+\boldsymbol{A}^{\mathrm{T}}\boldsymbol{P}+\frac{\varepsilon_1+\varepsilon_2}{\varepsilon_1\varepsilon_2}\boldsymbol{P}\boldsymbol{P}\right)\tilde{\boldsymbol{x}}\\ &+(c_1+c_2)||\tilde{\boldsymbol{x}}||^2+(c_3+c_4)||\tilde{\boldsymbol{x}}||\\ \le&-\|\tilde{\boldsymbol{x}}\|\Big((c_6-c_1-c_2)\|\tilde{\boldsymbol{x}}\|-(c_3+c_4)\Big),\end{aligned}\tag{33}$$

where $c_6 = -\lambda_{\max}\left(\boldsymbol{P}\boldsymbol{A}+\boldsymbol{A}^{\mathrm{T}}\boldsymbol{P}+\frac{\varepsilon_1+\varepsilon_2}{\varepsilon_1\varepsilon_2}\boldsymbol{P}\boldsymbol{P}\right)$. It can be seen that inequality (33) is a quadratic term, meaning that there exists a region $\Omega_1 : \{\|\tilde{\boldsymbol{x}}\|\big|\|\tilde{\boldsymbol{x}}\| \le R_1\}$, where

$$R_1 = \frac{c_3+c_4}{c_6-c_1-c_2}.\tag{34}$$

Remark 4 It can be seen that once the error vector is out of the radius (i.e., $\tilde{\boldsymbol{x}} \notin \Omega_1$), then $\dot{V}_1 < 0$ and it will asymptotically force the error variable convergence into the domain Ω_1. This implies that Ω_1 is an attraction region for observation errors. Note that the convergence radius is not constant, but related to the states and control parameters, and the radius R_1 will decrease with decreasing errors.

Step 2: Consider a new EBLF for $\tilde{\boldsymbol{x}}_1$ as

$$V_2 = \Psi(l_a,\tilde{\boldsymbol{x}}_1) = l_a^2\left(\exp\left(\frac{\tilde{\boldsymbol{x}}_1^{\mathrm{T}}\tilde{\boldsymbol{x}}_1}{l_a^2-\tilde{\boldsymbol{x}}_1^{\mathrm{T}}\tilde{\boldsymbol{x}}_1}\right)-1\right).\tag{35}$$

Differentiating V_2 along the system trajectory gives

$$\dot{V}_2 = 2l_a\dot{l}_a\left(\mathrm{e}^{\gamma_a}-1-\gamma_a\bar{\gamma}_a\mathrm{e}^{\gamma_a}\right)+2\bar{\gamma}_a^2\mathrm{e}^{\gamma_a}\tilde{\boldsymbol{x}}_1^{\mathrm{T}}\dot{\tilde{\boldsymbol{x}}}_1,\tag{36}$$

where $\gamma_a = \frac{\tilde{\boldsymbol{x}}_1^{\mathrm{T}}\tilde{\boldsymbol{x}}_1}{l_a^2-\tilde{\boldsymbol{x}}_1^{\mathrm{T}}\tilde{\boldsymbol{x}}_1}$, $\bar{\gamma}_a = \frac{l_a^2}{l_a^2-\tilde{\boldsymbol{x}}_1^{\mathrm{T}}\tilde{\boldsymbol{x}}_1}$, and l_a is the predefined time varying error constraint function. In the case of $\dot{l}_a > 0$, one has

$$2l_a\dot{l}_a\left(\mathrm{e}^{\gamma_a}-1-\gamma_a\bar{\gamma}_a\mathrm{e}^{\gamma_a}\right) \le 2l_a\dot{l}_a\mathrm{e}^{\gamma_a}.\tag{37}$$

When $\dot{l}_a < 0$, it can be derived that

$$-2l_a(-\dot{l}_a)\left(\mathrm{e}^{\gamma_a}-1-\gamma_a\bar{\gamma}_a\mathrm{e}^{\gamma_a}\right) \le 2l_a(-\dot{l}_a)\bar{\gamma}_a^2\mathrm{e}^{\gamma_a}.\tag{38}$$

Combining inequalities (37) and (38) gives

$$2l_a\dot{l}_a\left(\mathrm{e}^{\gamma_a}-1-\gamma_a\bar{\gamma}_a\mathrm{e}^{\gamma_a}\right) \le 2c_7l_a^2\bar{\gamma}_a^2\mathrm{e}^{\gamma_a},\tag{39}$$

where $c_7 = \sup\left(\sqrt{|\dot{l}_a|^2/l_a^2}\right)$ is the settable parameter, which is the upper bound of $|\dot{l}_a/l_a|$. With Lemma 3, the following inequality holds:

$$\begin{aligned}-\tilde{\boldsymbol{x}}_1^{\mathrm{T}}\boldsymbol{v}_1 \le&-\alpha_1\Big(|\tilde{x}_{11}|^{2\cdot\frac{r_1+1}{2}}+|\tilde{x}_{12}|^{2\cdot\frac{r_1+1}{2}}+\dots\\ &+|\tilde{x}_{1n}|^{2\cdot\frac{r_1+1}{2}}\Big)\\ \le&-\alpha_1||\tilde{\boldsymbol{x}}_1||^{r_1+1}.\end{aligned}\tag{40}$$

Combining the dynamics of $\tilde{\boldsymbol{x}}_1$ and inequality (40) gives

$$\begin{aligned}&2\bar{\gamma}_a^2\mathrm{e}^{\gamma_a}\tilde{\boldsymbol{x}}_1^{\mathrm{T}}\dot{\tilde{\boldsymbol{x}}}_1\\ \le&2\bar{\gamma}_a^2\mathrm{e}^{\gamma_a}\tilde{\boldsymbol{x}}_1^{\mathrm{T}}\left((\boldsymbol{T}-\boldsymbol{K}_1)\tilde{\boldsymbol{x}}_1+\tilde{\boldsymbol{x}}_2-\boldsymbol{v}_1\right)\\ \le&-2c_8\bar{\gamma}_a^2\mathrm{e}^{\gamma_a}||\tilde{\boldsymbol{x}}_1||^2+2\bar{\gamma}_a^2\mathrm{e}^{\gamma_a}\big(||\tilde{\boldsymbol{x}}_1||||\tilde{\boldsymbol{x}}_2||-\alpha_1||\tilde{\boldsymbol{x}}_1||^{r_1+1}\big),\end{aligned}\tag{41}$$

where $c_8 = -\lambda_{\max}(\boldsymbol{T}-\boldsymbol{K}_1)$. From step 1, it can be seen that

$$\|\tilde{\boldsymbol{x}}_2\| \le \|\tilde{\boldsymbol{x}}\| \le R_1.\tag{42}$$

Meanwhile, note that $\|\tilde{\boldsymbol{x}}_2\|^{r_1+1} \ge \|\tilde{\boldsymbol{x}}_2\|$. Let $\alpha_1 = c_9 + R_1$, where c_9 is the positive gain. Substituting α_1 into inequality (41) gives

$$\begin{aligned}2\bar{\gamma}_a^2\mathrm{e}^{\gamma_a}\tilde{\boldsymbol{x}}_1^{\mathrm{T}}\dot{\tilde{\boldsymbol{x}}}_1 \le&-2c_8\bar{\gamma}_a^2\mathrm{e}^{\gamma_a}||\tilde{\boldsymbol{x}}_1||^2\\ &-2c_9\bar{\gamma}_a^2\mathrm{e}^{\gamma_a}||\tilde{\boldsymbol{x}}_1||^{r_1+1}.\end{aligned}\tag{43}$$

Substituting inequalities (43) and (39) into Eq. (36), one has

$$\dot{V}_2 \le 2\bar{\gamma}_a^2\mathrm{e}^{\gamma_a}\left(c_7l_a^2-c_8||\tilde{\boldsymbol{x}}_1||^2-c_9||\tilde{\boldsymbol{x}}_1||^{r_1+1}\right).\tag{44}$$

Letting $c_8 \ge \frac{c_7l_a^2+c_{10}||\tilde{\boldsymbol{x}}_1||^2}{||\tilde{\boldsymbol{x}}_1||^2+\varepsilon_0}$, where ε_0 is a small positive scalar to avoid singularity and c_{10} is the positive feedback gain, Eq. (44) can be further deduced as

$$\begin{aligned}\dot{V}_2 \le&-2c_{10}\bar{\gamma}_a^2\mathrm{e}^{\gamma_a}||\tilde{\boldsymbol{x}}_1||^2-2c_9\bar{\gamma}_a^2\mathrm{e}^{\gamma_a}||\tilde{\boldsymbol{x}}_1||^{r_1+1}\\ \le&-2c_{10}(V_2)^{1/2}\left(\frac{\gamma_a}{\gamma_a+1}\right)^{1/2}\\ &-2c_9\mathrm{e}^{\frac{\gamma_a(1-r_1)}{2}}V_2^{\frac{(1+r_1)}{2}}\left(\frac{\gamma_a}{\gamma_a+1}\right)^{\frac{(1+r_1)}{2}}.\end{aligned}\tag{45}$$

To demonstrate fixed-time convergence, two new sets are defined as

$$\begin{cases} \Omega_2 : \{||\tilde{\boldsymbol{x}}_1|| \big| ||\tilde{\boldsymbol{x}}_1|| \le l_a\}, \\ \Omega_3 : \{\|\tilde{\boldsymbol{x}}_1\| \big| \|\tilde{\boldsymbol{x}}_1\| \le \sqrt{k_1} l_a\}, \end{cases} \tag{46}$$

where $0 \le k_1 \le 1$ is the defined auxiliary variable named the contraction factor. When the error state $\|\tilde{\boldsymbol{x}}_1\| \in \Omega_2 \setminus \Omega_3$, it can be obtained that

$$\gamma_a \ge \frac{k_1}{1-k_1}, \quad \frac{\gamma_a}{\gamma_a+1} \ge k_1. \tag{47}$$

Thus, inequality (45) can be further simplified as

$$\dot{V}_2 \le -2c_{10}k_1^{\frac{1}{2}}V_2^{\frac{1}{2}} - 2c_9 k_1^{\frac{r_1+1}{2}} \mathrm{e}^{\frac{\gamma_a(1-r_1)}{2}} V_2^{\frac{r_1+1}{2}}. \tag{48}$$

It can be seen that the derivative of the Lyapunov function remains negative when $\|\tilde{\boldsymbol{x}}_1\| \in \Omega_2 \setminus \Omega_3$, which indicates that the error $\|\tilde{\boldsymbol{x}}_1\|$ will decrease asymptotically when $\tilde{\boldsymbol{x}}_1$ is out of Ω_3. Meanwhile, with the fixed-time convergence property of Lemma 1, the velocity estimation error $\|\tilde{\boldsymbol{x}}_1\|$ will be driven to the boundary of Ω_3 and Ω_2 in T_1, where Ω_3 is a small vicinity of $\tilde{\boldsymbol{x}}_1 = \boldsymbol{0}$ with properly selected k_1. Moreover, the attraction region Ω_3 is continuously shrinking with the decreasing k_1 and will eventually approach zero in T_2. The convergence time T_1 is represented as

$$T_1 \le \frac{2}{c_{11}\zeta} + \frac{2}{c_{12}\zeta(r_1-1)}, \tag{49}$$

where $c_{11} = 2c_{10}k_1^{\frac{1}{2}}$ and $c_{12} = 2c_9 k_1^{(r_1+1)/2}\mathrm{e}^{\frac{\gamma_a(1-r_1)}{2}}$ are positive scalars and $0 < \zeta < 1$.

Remark 5 Note that Ω_1 in step 1 is only a rough attraction region of asymptotical stability. To achieve higher estimation accuracy, we further reduce the error domain to Ω_3 by incorporating EBLF with the contraction factor. Note that Ω_3 is an attraction region for velocity estimation error $\tilde{\boldsymbol{x}}_1$ and the area size is directly related to the contraction factor k_1. Moreover, the contraction factor k_1 decreases with decreasing $\tilde{\boldsymbol{x}}_1$, and eventually drives the error to zero in T_2. Therefore, the total convergence time T_{s1} includes state vector convergence time T_1 and attraction region contraction time T_2.

Step 3: This part presents the proof of fixed-time convergence of $\tilde{\boldsymbol{x}}_2$ with prescribed constraint l_b. Choose the candidate EBLF as follows:

$$V_3 = \Psi(l_b, \tilde{\boldsymbol{x}}_2) + \mathrm{tr}(\widetilde{\boldsymbol{W}}\widetilde{\boldsymbol{W}}^{\mathrm{T}}(\boldsymbol{\eta}^{\mathrm{T}})^{-1}). \tag{50}$$

Taking the first derivative of V_3 with respect to time gives

$$\begin{aligned} \dot{V}_3 \le & 2l_b\dot{l}_b\left(\mathrm{e}^{\gamma_b} - 1 - \gamma_b\bar{\gamma}_b\mathrm{e}^{\gamma_b}\right) + 2\bar{\gamma}_b^2\mathrm{e}^{\gamma_b}\tilde{\boldsymbol{x}}_2^{\mathrm{T}}\dot{\tilde{\boldsymbol{x}}}_2 \\ & + 2\mathrm{tr}\left(\widetilde{\boldsymbol{W}}^{\mathrm{T}}\dot{\widetilde{\boldsymbol{W}}}\left(\boldsymbol{\eta}^{\mathrm{T}}\right)^{-1}\right), \end{aligned} \tag{51}$$

where $\gamma_b = \dfrac{\tilde{\boldsymbol{x}}_2^{\mathrm{T}}\tilde{\boldsymbol{x}}_2}{l_b^2 - \tilde{\boldsymbol{x}}_2^{\mathrm{T}}\tilde{\boldsymbol{x}}_2}$ and $\bar{\gamma}_b = \dfrac{l_b^2}{l_b^2 - \tilde{\boldsymbol{x}}_2^{\mathrm{T}}\tilde{\boldsymbol{x}}_2}$. The first term $2l_b\dot{l}_b(\mathrm{e}^{\gamma_b} - 1 - \gamma_b\bar{\gamma}_b\mathrm{e}^{\gamma_b})$ can be scaled as follows with the same analysis in step 2:

$$2l_b\dot{l}_b(\mathrm{e}^{\gamma_b} - 1 - \gamma_b\bar{\gamma}_b\mathrm{e}^{\gamma_b}) \le 2c_{14}l_b^2\bar{\gamma}_b^2\mathrm{e}^{\gamma_b}, \tag{52}$$

where $c_{14} = \sqrt{\frac{|\dot{l}_b|^2}{|l_b|^2}}$ is the selectable variable. Note that from step 2, one can obtain $\tilde{\boldsymbol{x}}_1 = \boldsymbol{0}$ and $\dot{\tilde{\boldsymbol{x}}}_1 = \boldsymbol{0}$ when $t > T_1 + T_2$, which further results in

$$\tilde{\boldsymbol{x}}_2 = \boldsymbol{v}. \tag{53}$$

Substituting the above equation into the term $\tilde{\boldsymbol{x}}_2^{\mathrm{T}}\dot{\tilde{\boldsymbol{x}}}_2$, one has

$$\begin{aligned} \tilde{\boldsymbol{x}}_2^{\mathrm{T}}\dot{\tilde{\boldsymbol{x}}}_2 = & -\tilde{\boldsymbol{x}}_2^{\mathrm{T}}\boldsymbol{T}\tilde{\boldsymbol{x}}_2 - \tilde{\boldsymbol{x}}_2^{\mathrm{T}}\boldsymbol{H}^{-1}\left(\dot{\boldsymbol{H}} + \boldsymbol{C}\right)\tilde{\boldsymbol{x}}_2 \\ & - \tilde{\boldsymbol{x}}_2^{\mathrm{T}}\boldsymbol{H}^{-1}\left(\hat{\boldsymbol{C}} - \dot{\boldsymbol{C}}\right)\dot{\boldsymbol{q}} - \tilde{\boldsymbol{x}}_2^{\mathrm{T}}(\hat{\boldsymbol{Q}} - \boldsymbol{Q}) - \tilde{\boldsymbol{x}}_2^{\mathrm{T}}\boldsymbol{v}_2. \end{aligned} \tag{54}$$

Note that

$$-\tilde{\boldsymbol{x}}_2^{\mathrm{T}}\boldsymbol{H}^{-1}\left(\hat{\boldsymbol{C}} - \dot{\boldsymbol{C}}\right)\dot{\boldsymbol{q}} \le \frac{1}{\underline{\lambda}_{\mathrm{H}}}||\tilde{\boldsymbol{x}}_2||^2. \tag{55}$$

With the Young inequality and Eq. (20), one has

$$\begin{aligned} & \tilde{\boldsymbol{x}}_2^{\mathrm{T}}(\hat{\boldsymbol{Q}} - \boldsymbol{Q}) = \tilde{\boldsymbol{x}}_2^{\mathrm{T}}(\widetilde{\boldsymbol{W}}^{\mathrm{T}}\boldsymbol{\varphi}(\dot{\boldsymbol{q}}, \hat{\dot{\boldsymbol{q}}}) + \boldsymbol{N} - \boldsymbol{\epsilon}^*) \\ \le & \tilde{\boldsymbol{x}}_2^{\mathrm{T}}\widetilde{\boldsymbol{W}}^{\mathrm{T}}\boldsymbol{\varphi}\Big(\dot{\boldsymbol{q}}, \hat{\dot{\boldsymbol{q}}}\Big) + \frac{1}{\varepsilon_2}\tilde{\boldsymbol{x}}_2^{\mathrm{T}}\tilde{\boldsymbol{x}}_2 + \varepsilon_2 b^2||\tilde{\boldsymbol{x}}_2||^2 + \epsilon_N||\tilde{\boldsymbol{x}}_2||. \end{aligned} \tag{56}$$

Similar to the analysis in inequality (40), it can be obtained that

$$\begin{aligned} -\tilde{\boldsymbol{x}}_2^{\mathrm{T}}\boldsymbol{v}_2 = & -\alpha_2\tilde{\boldsymbol{x}}_2^{\mathrm{T}}\mathrm{sig}\left(\boldsymbol{v}_1\right)^{r_2} - \alpha_3\tilde{\boldsymbol{x}}_2^{\mathrm{T}}\mathrm{sig}\left(\boldsymbol{v}_1\right)^{r_3} \\ \le & -\alpha_2||\tilde{\boldsymbol{x}}_2||^{r_2+1} - \alpha_3||\tilde{\boldsymbol{x}}_2||^{r_3+1}. \end{aligned} \tag{57}$$

Combining inequalities (55)–(57) with Eq. (54) leads to

$$\begin{aligned} \tilde{\boldsymbol{x}}_2^{\mathrm{T}}\dot{\tilde{\boldsymbol{x}}}_2 \le & -\left(c_{13} - \frac{1}{\underline{\lambda}_{\mathrm{H}}} - \varepsilon_2 b^2\right)||\tilde{\boldsymbol{x}}_2||^2 - \alpha_2||\tilde{\boldsymbol{x}}_2||^{r_2+1} \\ & - \alpha_3||\tilde{\boldsymbol{x}}_2||^{r_3+1} + \epsilon_N||\tilde{\boldsymbol{x}}_2|| + \tilde{\boldsymbol{x}}_2^{\mathrm{T}}\widetilde{\boldsymbol{W}}^{\mathrm{T}}\boldsymbol{\varphi}(\dot{\boldsymbol{q}}, \hat{\dot{\boldsymbol{q}}}) - \alpha_4\|\tilde{\boldsymbol{x}}_2\|, \end{aligned} \tag{58}$$

where $c_{13} = -\lambda_{\max}\left(\boldsymbol{T}+\boldsymbol{H}^{-1}(\dot{\boldsymbol{H}}+\boldsymbol{C})-\dfrac{1}{\varepsilon_2}\boldsymbol{I}\right)$. Since $\boldsymbol{T}$ is the chosen transformation matrix, $c_{13}-\frac{1}{\lambda_{\mathrm{H}}}-\varepsilon_2 b^2>0$ can be guaranteed with properly selected parameters and it further leads to

$$\begin{aligned}\tilde{\boldsymbol{x}}_2^{\mathrm{T}}\dot{\tilde{\boldsymbol{x}}}_2\leq&-\alpha_2||\tilde{\boldsymbol{x}}_2||^{r_2+1}-\alpha_3||\tilde{\boldsymbol{x}}_2||^{r_3+1}+\epsilon_N||\tilde{\boldsymbol{x}}_2||\\&-\alpha_4\|\tilde{\boldsymbol{x}}_2\|+\tilde{\boldsymbol{x}}_2^{\mathrm{T}}\widetilde{\boldsymbol{W}}^{\mathrm{T}}\boldsymbol{\varphi}\left(\dot{\boldsymbol{q}},\hat{\dot{\boldsymbol{q}}}\right),\end{aligned}\tag{59}$$

where α_2,α_3, and α_4 are the optional feedback gains satisfying $\alpha_2\geq\dfrac{c_{14}l_b^2+c_{15}||\tilde{\boldsymbol{x}}_2||^{r_2+1}}{||\tilde{\boldsymbol{x}}_2||^{r_2+1}+\varepsilon_0}$ and $\alpha_4\geq\epsilon_N$.

Substituting inequalities (52) and (59) into inequality (51) gives

$$\begin{aligned}\dot{V}_3\leq&-2c_{15}\bar{\gamma}_b^2\mathrm{e}^{\gamma_b}||\tilde{\boldsymbol{x}}_2||^{r_2+1}-2c_{16}\bar{\gamma}_b^2\mathrm{e}^{\gamma_b}||\tilde{\boldsymbol{x}}_2||^{r_3+1}\\&+2\bar{\gamma}_b^2\mathrm{e}^{\gamma_b}\tilde{\boldsymbol{x}}_2^{\mathrm{T}}\widetilde{\boldsymbol{W}}^{\mathrm{T}}\boldsymbol{\varphi}(\dot{\boldsymbol{q}},\hat{\dot{\boldsymbol{q}}})+2\mathrm{tr}(\widetilde{\boldsymbol{W}}^{\mathrm{T}}\dot{\widetilde{\boldsymbol{W}}}(\boldsymbol{\eta}^{\mathrm{T}})^{-1}),\end{aligned}\tag{60}$$

where c_{15} and $c_{16}=\alpha_3$ are positive scalars. From step 1, one can obtain

$$\|\tilde{\boldsymbol{x}}_2\|^2\leq\|\tilde{\boldsymbol{x}}\|^2\leq R_1.\tag{61}$$

Together with the adaptive law for the weight matrix of RBFNNs, one has

$$\begin{aligned}&2\bar{\gamma}_b^2\mathrm{e}^{\gamma_b}\tilde{\boldsymbol{x}}_2^{\mathrm{T}}\widetilde{\boldsymbol{W}}^{\mathrm{T}}\boldsymbol{\varphi}(\dot{\boldsymbol{q}},\hat{\dot{\boldsymbol{q}}})+2\mathrm{tr}(\widetilde{\boldsymbol{W}}^{\mathrm{T}}\dot{\widetilde{\boldsymbol{W}}}(\boldsymbol{\eta}^{\mathrm{T}})^{-1})\\\leq&2\bar{\gamma}_b^2\mathrm{e}^{\gamma_b}\tilde{\boldsymbol{x}}_2^{\mathrm{T}}\widetilde{\boldsymbol{W}}^{\mathrm{T}}\boldsymbol{\varphi}(\dot{\boldsymbol{q}},\hat{\dot{\boldsymbol{q}}})-2\bar{\gamma}_b^2\mathrm{e}^{\gamma_b}\tilde{\boldsymbol{x}}_2^{\mathrm{T}}\widetilde{\boldsymbol{W}}^{\mathrm{T}}\boldsymbol{\varphi}(\dot{\boldsymbol{q}},\hat{\dot{\boldsymbol{q}}})\\\leq&0.\end{aligned}\tag{62}$$

Thus, inequality (60) can be further deduced as

$$\begin{aligned}\dot{V}_3\leq&-2c_{15}\bar{\gamma}_b^2\mathrm{e}^{\gamma_b}||\tilde{\boldsymbol{x}}_2||^{r_2+1}-2c_{16}\bar{\gamma}_b^2\mathrm{e}^{\gamma_b}||\tilde{\boldsymbol{x}}_2||^{r_3+1}\\\leq&-2c_{15}\left(l_b^2\left(\mathrm{e}^{\gamma_b}-1\right)\right)^{\frac{r_2+1}{2}}\left(\frac{\gamma_b}{\gamma_b+1}\right)^{\frac{r_2+1}{2}}\\&-2c_{16}\mathrm{e}^{\frac{\gamma_b(1-r_3)}{2}}\left(l_b^2\left(\mathrm{e}^{\gamma_b}-1\right)\right)^{\frac{r_3+1}{2}}\left(\frac{\gamma_b}{\gamma_b+1}\right)^{\frac{r_3+1}{2}}.\end{aligned}\tag{63}$$

Similar to step 2, two new sets are defined as follows to prove the error convergence:

$$\begin{cases}\Omega_4=\{\|\tilde{\boldsymbol{x}}_2\|\big|\|\tilde{\boldsymbol{x}}_2\|\leq l_b\},\\\Omega_5=\{\|\tilde{\boldsymbol{x}}_2\|\big|\|\tilde{\boldsymbol{x}}_2\|\leq\sqrt{k_2}l_b\},\end{cases}\tag{64}$$

where $0<k_2\leq1$ is the contraction factor and the definitions lead to

$$\begin{aligned}\dot{V}_3\leq&-2c_{15}\Psi\left(l_b,\tilde{\boldsymbol{x}}_2\right)^{\frac{r_2+1}{2}}k_2^{\frac{r_2+1}{2}}\\&-2c_{17}\Psi\left(l_b,\tilde{\boldsymbol{x}}_2\right)^{\frac{r_3+1}{2}}k_2^{\frac{r_3+1}{2}}\\\leq&-c_{18}V_3^{\frac{r_2+1}{2}}-c_{19}V_3^{\frac{r_3+1}{2}},\end{aligned}\tag{65}$$

where $c_{17}=c_{16}\inf\left(\mathrm{e}^{\frac{\gamma_b(1-r_3)}{2}}\right)$, $c_{18}=2c_{15}k_2^{\frac{r_2+1}{2}}$, and $c_{19}=2c_{17}k_2^{\frac{r_3+1}{2}}$.

With Lemma 1, it can be obtained that the estimation error $\tilde{\boldsymbol{x}}_2$ will approach the boundary of Ω_4 and Ω_5 within fixed time T_3 under the prescribed constraint l_b.

$$T_3\leq\frac{2}{c_{18}\zeta(1-r_2)}+\frac{2}{c_{19}\zeta(r_3-1)}.\tag{66}$$

Moreover, by decreasing the chosen contraction factor k_2, the vicinity Ω_5 is further reduced and eventually approaches zero in T_4. This implies that the acceleration estimation error trajectory $\tilde{\boldsymbol{x}}_2$ will shrink from Ω_1 to Ω_5 in finite time $T_{\mathrm{s}2}=T_3+T_4$. Therefore, the total settling time of the proposed observer is $T_{\mathrm{ob}}=T_{\mathrm{s}1}+T_{\mathrm{s}2}$.

Remark 6 The initial states for the robotic exoskeleton are not always available, especially when interacting with human limbs. Note that the total convergence time in the proposed observer is irrelevant to the initial states, which relaxes the requirements in the conventional finite-time observer. Moreover, the lumped disturbance is assumed to be completely unknown without any assumptions in this study, which is more general and robust in practice. Furthermore, by combining the proposed exponential-type Lyapunov function with the contraction factor, the acceleration estimation accuracy, fixed-time convergence, initial state irrelevance, and error-constrained control can be guaranteed simultaneously.

5 Simulation and experimental results

5.1 Simulation

Compared with traditional multi-link robots, the essential characteristic of the robotic exoskeleton is the human-in-the-loop model, where the robotic machine is directly coupled with the human body. The exoskeleton dynamics can not only be affected by the internal disturbances from the driving system, but also strongly disturbed by the unpredictable ever-changing body movements. Therefore, we adopt the same two-link robot dynamics, but couple with a strong disturbance as the exoskeleton platform. The proposed acceleration observer scheme is implemented for each joint with nine different initial state values to validate its unique properties, i.e.,

fixed-time convergence and constrained observation errors. The parameters of the robots are listed in Table 1. The simulated human-exoskeleton interaction disturbance is assumed to be related to the joint angular velocity and acceleration, which is a relatively huge disturbance for the robot dynamics. It is denoted as

$$\boldsymbol{\delta}(\dot{\boldsymbol{q}}, \ddot{\boldsymbol{q}}) = 0.3\dot{\boldsymbol{q}} + 0.15\ddot{\boldsymbol{q}}, \tag{67}$$

where $\dot{\boldsymbol{q}} = [\dot{q}_1, \dot{q}_2]$ and $\ddot{\boldsymbol{q}} = [\ddot{q}_1, \ddot{q}_2]$.

Table 1 Parameters of the robotic exoskeleton

Parameter	Value	
	Link 1	Link 2
Length of link (m)	1	1
Weight of link (kg)	1	1
Center-of-gravity position of link (m)	0.5	0.5

The two-link robotic system is initially set at a static level as shown in Fig. 3, and it will fall free under gravity effects. In this process, a simple damping controller, i.e., $\boldsymbol{\tau} = -0.5\dot{\boldsymbol{q}}$, is applied to the joints to simulate the rotation friction. The parameters of the proposed observer are listed in Table 2. To confirm fixed-time convergence and initial state independence, nine cases of initial state values are selected as Eq. (68), which are uniformly distributed around the ground truth.

$$\hat{\dot{\boldsymbol{q}}}(0) = \begin{cases} [-19, 39.2]^{\mathrm{T}}, & \text{case 1}, \\ [-16.5, 41.7]^{\mathrm{T}}, & \text{case 2}, \\ \quad\vdots & \\ [-29, 29.2]^{\mathrm{T}}, & \text{case 9}. \end{cases} \tag{68}$$

Figs. 4 and 5 show the velocity and acceleration observation tracking performance under the nine cases, respectively. It can be seen that observed velocities and accelerations show a rapid convergence

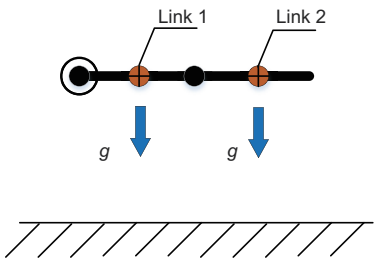

Fig. 3 Schematic diagram of the simulation environment

Table 2 Parameters of the acceleration observer in simulation

Parameter	Value
l_a	0.2
l_b	40
r_1	1.2
r_2	0.3
r_3	1.2
α_1	100
α_2	2
α_3	2
α_4	10
$\boldsymbol{K}_1$	diag(20,50)
$\boldsymbol{K}_2$	diag(20,50)
$\boldsymbol{T}$	diag(0.01,0.01)
$\boldsymbol{\eta}$	diag(0.05,0.05)

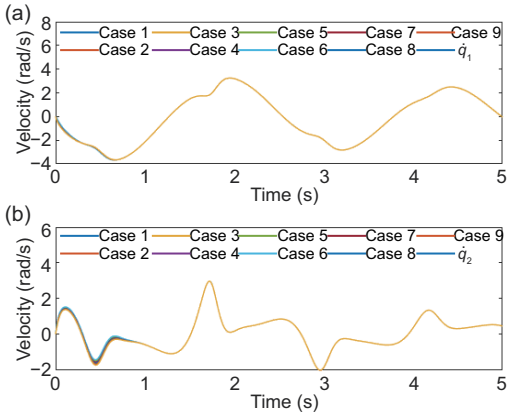

Fig. 4 Trajectories of observed and actual velocities: (a) observed velocity $\hat{\dot{q}}_1$ and actual velocity $\dot{q}_1$; (b) observed velocity $\hat{\dot{q}}_2$ and actual velocity $\dot{q}_2$

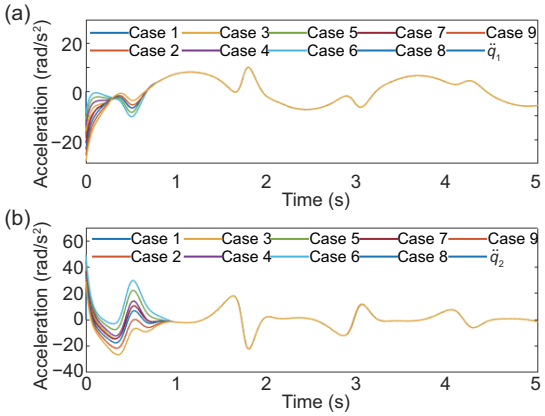

Fig. 5 Trajectories of observed and actual accelerations: (a) observed acceleration $\hat{\ddot{q}}_1$ and actual acceleration $\ddot{q}_1$; (b) observed acceleration $\hat{\ddot{q}}_2$ and actual acceleration $\ddot{q}_2$

rate at initial time and are fully capable of tracking time-varying trajectories thereafter. In particular, all the trajectories achieve complete tracking in the

same fixed time. Figs. 6 and 7 show the observation errors of joint velocity and acceleration, respectively. It can be seen that these error trajectories are different at the starting time, where more deviation of initial states will induce larger overshoots; however, they all converge to zero at the same time. The red dotted lines in Figs. 6 and 7 are the predefined bounds for observation errors, and it can be seen that the observation velocity errors never exceed the predefined constraints even in the convergent transient process, which further illustrates the effectiveness of the state constraint of the proposed EBLF.

Fig. 8 shows the disturbance approximation performance via RBFNNs. It can be seen that the designed RBFNNs with adaptive laws are capable of estimating most parts of the disturbance. Although RBFNNs cannot guarantee perfect estimation and there still exist some errors, especially at the spike points, the errors are quite small compared with raw disturbance and limited within a fixed range from Fig. 9. In the proposed scheme, the sliding mode control law can totally suppress these uncompensated parts.

The above simulation results verify the unique properties (i.e., fixed-time convergence, initial state irrelevance, high accuracy, and perfect disturbance suppression) of the proposed algorithm preliminarily. Also, the acceleration reconstruction performs as expected from these figures in terms of both the

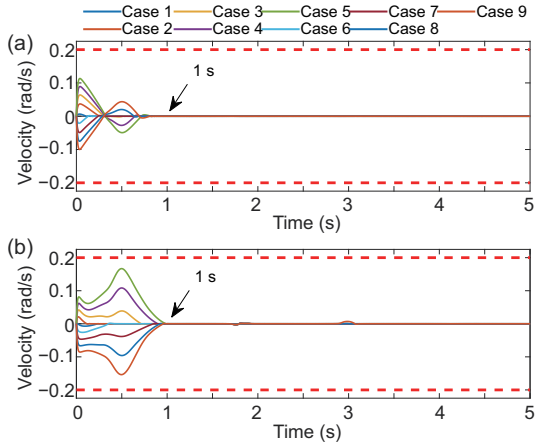

Fig. 6 Velocity observation errors of $\dot{q}_1$ (a) and $\dot{q}_2$ (b)
References to color refer to the online version of this figure

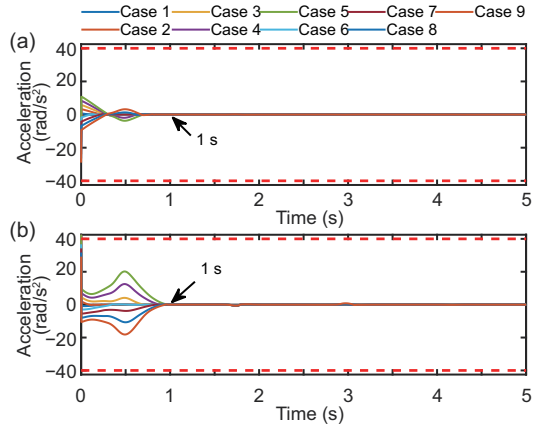

Fig. 7 Acceleration observation errors of $\ddot{q}_1$ (a) and $\ddot{q}_2$ (b)
References to color refer to the online version of this figure

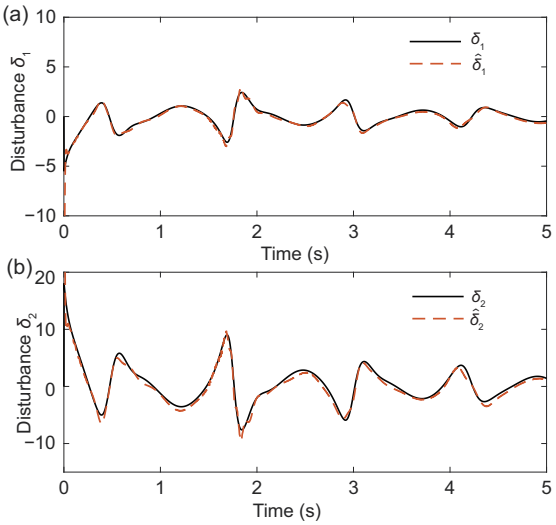

Fig. 8 Disturbance estimation performance via RBFNNs: (a) disturbance estimation of δ_1; (b) disturbance estimation of δ_2

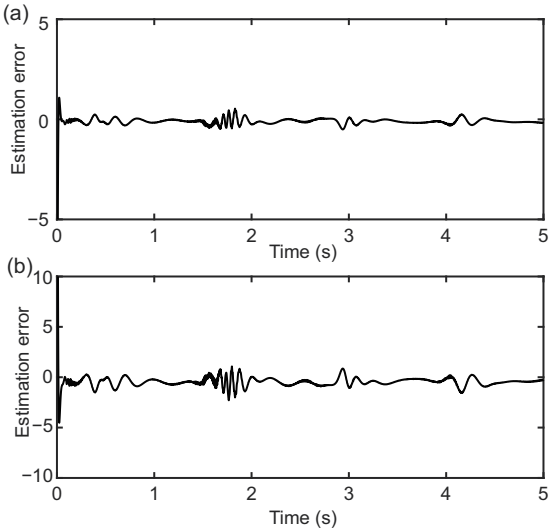

Fig. 9 Disturbance estimation errors via RBFNNs: (a) disturbance estimation error of δ_1; (b) disturbance estimation error of δ_2

static and dynamic accuracies. However, the system is continuous and the model is accurate in the simulation environment, which is impossible in the physical exoskeleton platform. Therefore, it has to be tested further in physical experiments to validate the properties and robustness.

5.2 Experiments

As shown in Fig. 1, the developed hip exoskeleton has one active degree for each leg, which provides flexion and extension forces around the hip to realize movement assistance. In this system, the angular position and velocity of the joint can be easily and directly obtained from the encoder but the acceleration remains unknown. In this part, we use the proposed algorithm to reconstruct the unmeasurable acceleration signal from existing information.

A healthy human subject was recruited to carry out an acceleration reconstruction experiment with the developed hip assistance exoskeleton. To make the results convincing, nine cases of initial state values and different activities of daily living, including squatting and level walking, were considered in this experiment. In these test cases, the walking motion is more dynamic, while squatting is more static; these two scenarios are used to demonstrate the static-dynamic performance of acceleration estimation. In addition, the quantitative comparison results with linear differential observers are presented to further demonstrate the superiority of the proposed scheme. The parameters of the proposed scheme are listed in Table 3.

Similar to the simulation, nine cases of uniformly distributed initial state values are selected as Eq. (69) to validate the fixed-time convergence property:

$$\hat{\dot{q}}(0)=\begin{cases}-40, & \text{case 1},\\ -30, & \text{case 2},\\ \quad\vdots & \\ 40, & \text{case 9}.\end{cases} \tag{69}$$

Table 3 Parameters of the acceleration observer in experiments

Parameter	Value
l_a	0.3
l_b	40
r_1	1.2
r_2	0.3
r_3	1.2
α_1	100
α_2	50
α_3	150
α_4	150
K_1	10
K_2	10
$\boldsymbol{T}$	diag(0.01,0.01)
$\boldsymbol{\eta}$	diag(0.05,0.05)

5.2.1 Walking experiments

One complete experimental gait cycle with robotic exoskeleton is shown in Fig. 10 and two cycles of walking gait data were presented in the following figures. The velocity/acceleration tracking performance and errors are plotted in Figs. 11–14.

The velocity and acceleration tracking results for these nine cases show that the proposed scheme has a high convergence rate at the starting time and is fully capable of tracking strongly disturbed signals. In addition, it can be seen from the enlarged figures that all these tracking trajectories converge at the same fixed time 0.1 s, which is irrelevant to the initial state values. Also, the reconstruction errors from Figs. 12 and 14 validate the fixed-time convergence property. The predefined error bounds in Figs. 12 and 14 are presented with red dotted lines. It can be seen that both the velocity and

Fig. 10 Walking assistance with robotic exoskeleton

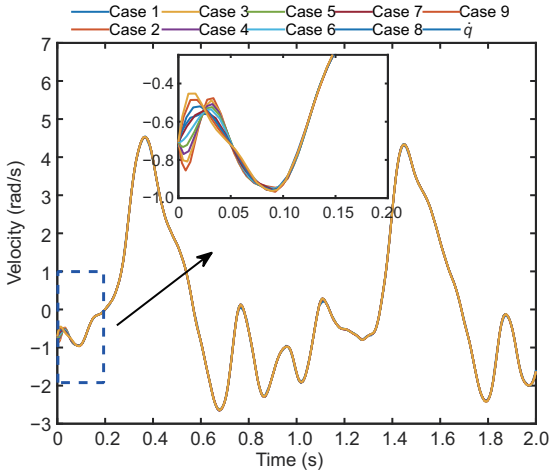

Fig. 11 Velocity tracking performance via the proposed scheme in the walking experiments

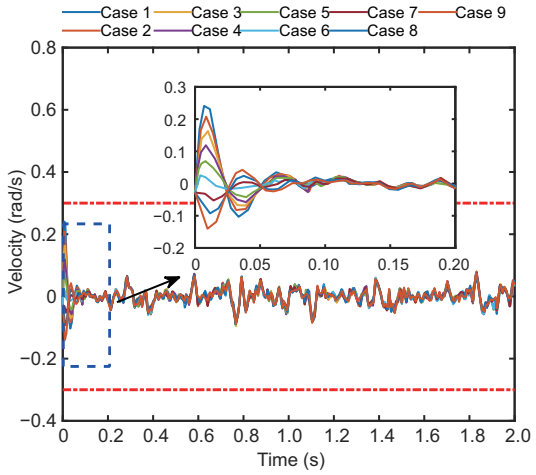

Fig. 12 Velocity reconstruction errors via the proposed scheme in the walking experiments

References to color refer to the online version of this figure

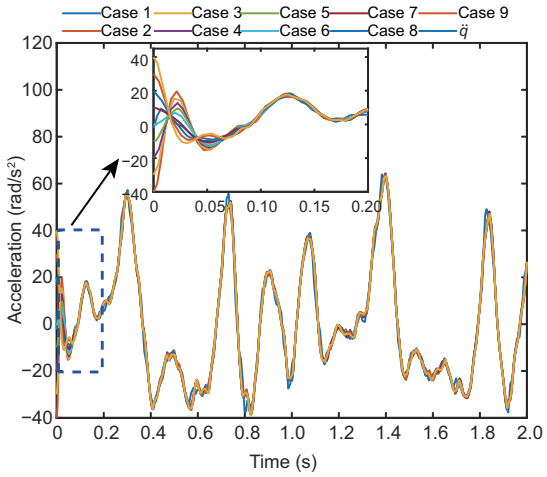

Fig. 13 Acceleration tracking performance via the proposed scheme in the walking experiments

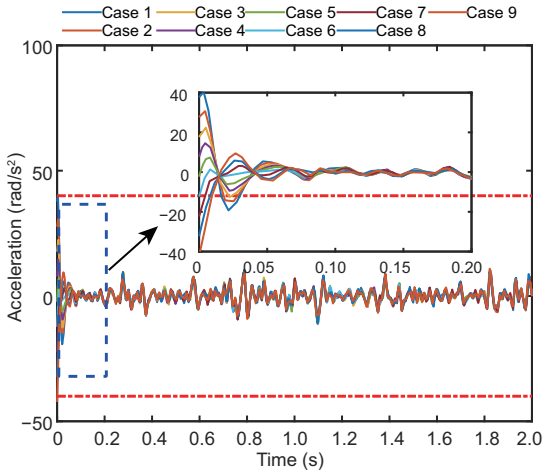

Fig. 14 Acceleration reconstruction errors via the proposed scheme in the walking experiments

References to color refer to the online version of this figure

acceleration reconstruction errors are limited in the predefined constraints. The convergence process is similar to the simulation; more deviation of the initial states will induce larger overshoot, but they all converge at the same time with the same predefined constraints. Note that, in contrast to the simulation, there still exist estimation errors in a steady process in these experiments. This might be the result of discrete sampling data and modeling uncertainties of physical systems. Fortunately, the static estimation errors are all limited in a small range under the predefined constraint, where the errors will decrease with the reduced constraint, and the errors are totally acceptable to the control accuracy for human-exoskeleton interaction.

To make the results convincing, a traditional linear differential observer was also implemented, whose mathematical form can be described as

$$\begin{cases} \dot{z} = -lz - l^2\dot{q}, \\ \hat{\ddot{q}} = z + l\dot{q}, \end{cases} \tag{70}$$

where z is the state variable and l represents the feedback gain. The results using linear observers are shown in Figs. 15 and 16. The accuracy of the estimated acceleration trajectory with actual signals is poor. It has a maximum error of 50.98 rad/s^2 at time 0.72 s, while all the errors approach zero at time 0.1 s with the proposed algorithm. Moreover, the estimated signal has a significant delay with ground truth, which will bring serious challenges in stability control.

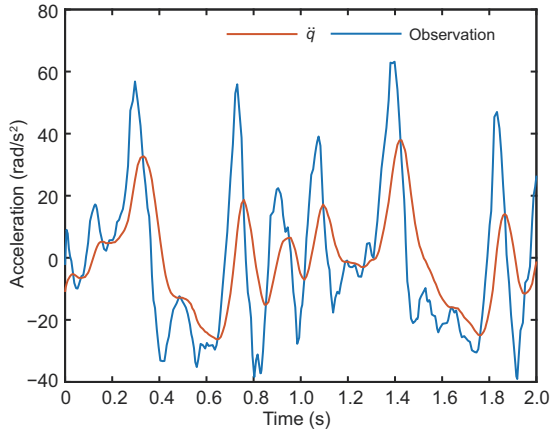

Fig. 15 Acceleration tracking performance via the linear observer in the walking experiments

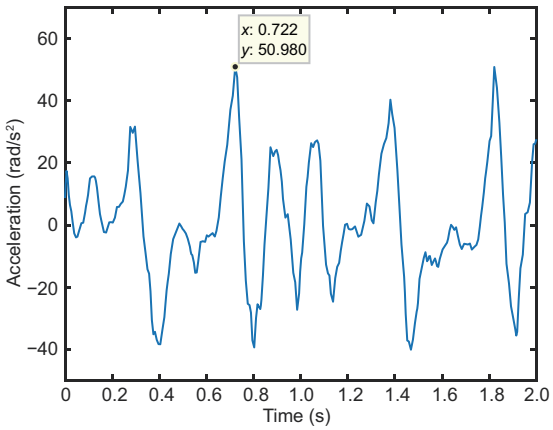

Fig. 16 Acceleration reconstruction errors via the linear observer in the walking experiments

5.2.2 Sit-to-stand experiments

One complete sit-to-stand cycle with exoskeleton assistance is shown in Fig. 17, where the subject performed a series of squatting actions in a slow manner. This experiment further verified the static-dynamic conversion performance of the proposed scheme. Similar to the above experiments, the angular accelerations were estimated with the proposed scheme and linear differential observer, respectively.

The velocity and acceleration tracking results are shown in Figs. 18 and 19, respectively, while the

Fig. 17 A sit-to-stand cycle with exoskeleton assistance

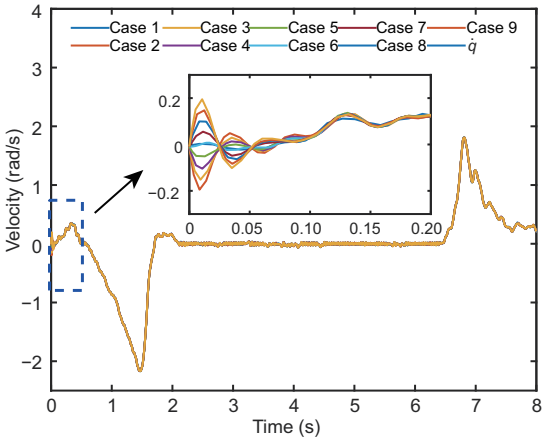

Fig. 18 Velocity tracking performance via the proposed scheme in the sit-to-stand experiments

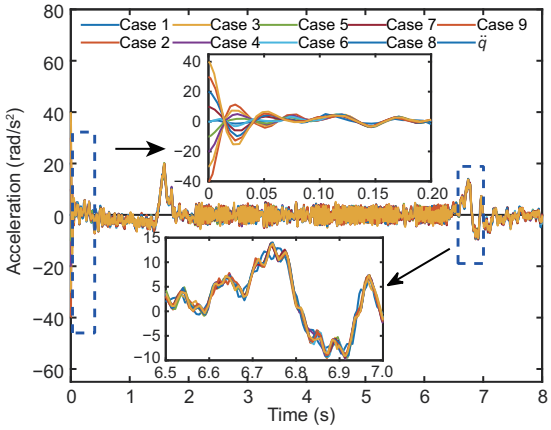

Fig. 19 Acceleration tracking performance via the proposed scheme in the sit-to-stand experiments

corresponding errors are presented in Figs. 20 and 21. The results demonstrate properties that are similar to those in the walking experiments. It shows perfect tracking capability with a high convergence rate and high accuracy, and all the estimation errors under different initial values approach zero in the same fixed time. Moreover, it can be seen that this estimation is still precise at the conversion points between static and dynamic states. Most importantly, the reconstruction errors are all constrained within the predefined bounds. Note that there still exist estimation errors during the whole process, especially at the static states. However, the errors are relatively small and completely acceptable to the exoskeleton system.

Figs. 22 and 23 show the estimation results from the linear differential observer. It can be seen that the observer is more like a low-pass filter to maintain the low-frequency components of acceleration. However, the high-frequency components are significant in a dynamical process like human movements, and the low-pass property will induce severe errors. From Fig. 23, the maximum estimation error reaches 9.9 rad/s^2 during squatting, which is totally unacceptable. Moreover, it shows a serious time delay at the conversion points and in the dynamic process.

The quantitative comparison results between the proposed scheme and the linear observer are presented in Table 4. The same zero initial state values were set for the two approaches and two parameters (i.e., root mean square error (RMSE) and maximum error) were selected as the evaluation criteria. From the data, it can be seen that the proposed scheme

Table 4 Performance comparison

Scenario	RMSE (rad/s^2)			Maximum error (rad/s^2)		
	Proposed scheme	Linear observer	Reduction	Proposed scheme	Linear observer	Reduction
Walking	3.15	18.85	82.29%	10.55	51.53	79.52%
Squatting	1.76	2.00	12.08%	4.31	9.98	56.75%

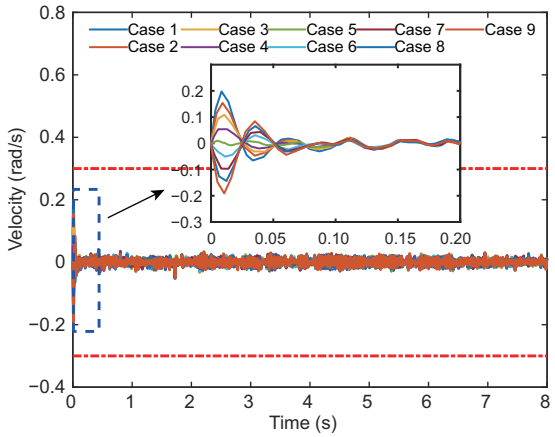

Fig. 20 Velocity reconstruction errors via the proposed scheme in the sit-to-stand experiments

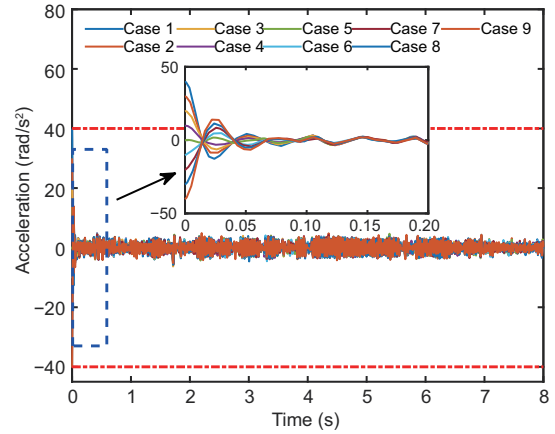

Fig. 21 Acceleration reconstruction errors via the proposed scheme in the sit-to-stand experiments

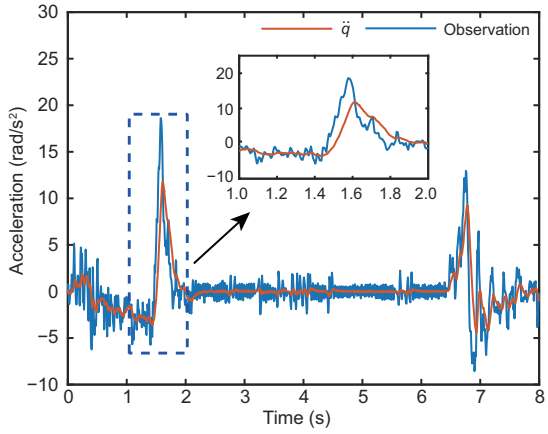

Fig. 22 Acceleration tracking performance via the linear observer in the sit-to-stand experiments

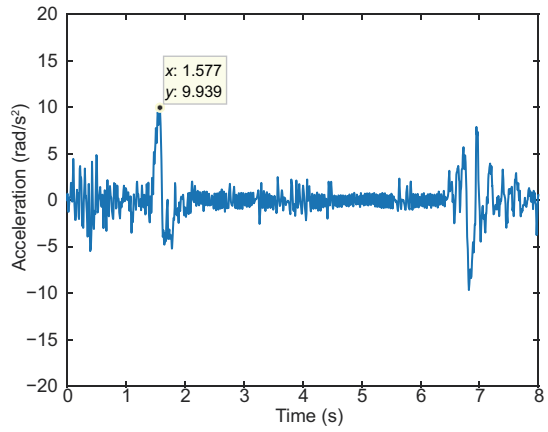

Fig. 23 Acceleration reconstruction errors via the linear observer in the sit-to-stand experiments

shows significantly reduced RMSE and maximum error during walking and squatting experiments. In the dynamic process of walking, RMSE and the maximum error decrease by 82.29% and 79.52%, respectively. Even in the static process of squatting movements, the acceleration estimation performance is still enhanced, but it is not as obvious as that in the walking experiments. In all, the data demonstrate comprehensive superiority of acceleration reconstruction.

In summary, both the simulation and physical experiments validate the unique properties of the proposed algorithm, i.e., fixed-time convergence, initial state irrelevance, high reconstruction accuracy, perfect disturbance suppression, and excellent static-dynamic performance. Compared with the linear differential observer, the estimation performance is strongly improved in dynamic motions like walking and is also enhanced in static motions like squatting, which account for most of the activities of daily living. Note that, different from the simulation, there still exist some errors in physical experiments due to the discrete sampling data and uncertainties of modeling. Therefore, it is recommended to adopt a high

sampling rate and a relatively accurate model when using this algorithm.

6 Conclusions

In this study, we have investigated the fixed-time acceleration estimation problem of the robotic exoskeleton system with prescribed error constraints. The proposed scheme has some unique properties, i.e., fixed-time convergence, initial state irrelevance, high reconstruction accuracy, perfect disturbance suppression, and excellent static-dynamic performance, which will contribute to developing better acceleration-dependent control algorithms. In theory, a novel EBLF has been proposed to handle the observation error constraints, providing an alternative barrier Lyapunov function template for constraint and non-constraint systems. Based on the EBLF, an adaptive acceleration observer has been further developed to achieve fixed-time acceleration observation, where RBFNNs were used to approximate the completely unknown lumped disturbances. Both the simulation and human subject experimental results validated the properties, and the superiority has been further highlighted with the quantitative comparison results.

Contributors

Tao XUE and Zi-wei WANG designed the research. Meng ZHANG processed the data. Ou BAI drafted the manuscript. Bin HAN helped organize the manuscript. Tao ZHANG revised and edited the final version.

Compliance with ethics guidelines

Tao XUE, Zi-wei WANG, Tao ZHANG, Ou BAI, Meng ZHANG, and Bin HAN declare that they have no conflict of interest.

The Ethics Committee of Tsinghua University had reviewed the experimental procedure and method, and approved this experiment (No. 20200014). Before the experiment, all subjects signed the informed written consent and agreed to participate in this experiment.

References

Abooee A, Moravej Khorasani M, Haeri M, 2017. Finite time control of robotic manipulators with position output feedback. *Int J Robust Nonl Contr*, 27(16):2982-2999. https://doi.org/10.1002/rnc.3721

Aguirre-Ollinger G, Colgate JE, Peshkin MA, et al., 2007. Active-impedance control of a lower-limb assistive exoskeleton. 10th Int Conf on Rehabilitation Robotics, p.188-195. https://doi.org/10.1109/icorr.2007.4428426

Chen Q, Cheng H, Yue C, et al., 2018. Dynamic balance gait for walking assistance exoskeleton. *Appl Bion Biomech*, 2018:7847014. https://doi.org/10.1155/2018/7847014

Chen S, Chen Z, Yao B, et al., 2017. Adaptive robust cascade force control of 1-DOF hydraulic exoskeleton for human performance augmentation. *IEEE/ASME Trans Mech*, 22(2):589-600. https://doi.org/10.1109/TMECH.2016.2614987

Dong TY, Zhang XL, Liu T, 2018. Artificial muscles for wearable assistance and rehabilitation. *Front Inform Technol Electron Eng*, 19(11):1303-1315. https://doi.org/10.1631/FITEE.1800618

Fei J, Ding H, 2012. Adaptive sliding mode control of dynamic system using RBF neural network. *Nonl Dynam*, 70(2):1563-1573. https://doi.org/10.1007/s11071-012-0556-2

He S, Lin D, 2018. Reliable spacecraft rendezvous without velocity measurement. *Acta Astron*, 144:52-60. https://doi.org/10.1016/j.actaastro.2017.12.016

He Y, Li N, Wang C, et al., 2019. Development of a novel autonomous lower extremity exoskeleton robot for walking assistance. *Front Inform Technol Electron Eng*, 20(3):318-329. https://doi.org/10.1631/FITEE.1800561

Hua CC, Yang Y, Guan X, 2013. Neural network-based adaptive position tracking control for bilateral teleoperation under constant time delay. *Neurocomputing*, 113:204-212. https://doi.org/10.1016/j.neucom.2013.01.016

Huo WG, Mohammed S, Amirat Y, et al., 2016. Active impedance control of a lower limb exoskeleton to assist sit-to-stand movement. Proc IEEE Int Conf on Robotics and Automation, p.3530-3536. https://doi.org/10.1109/ICRA.2016.7487534

Kang I, Hsu H, Young A, 2019. The effect of hip assistance levels on human energetic cost using robotic hip exoskeletons. *IEEE Robot Autom Lett*, 4(2):430-437. https://doi.org/10.1109/LRA.2019.2890896

Kazerooni H, Racine J, Huang LH, et al., 2005. On the control of the Berkeley lower extremity exoskeleton (BLEEX). Proc IEEE Int Conf on Robotics and Automation, p.4353-4360. https://doi.org/10.1109/ROBOT.2005.1570790

Kim H, Shin YJ, Kim J, 2017. Design and locomotion control of a hydraulic lower extremity exoskeleton for mobility augmentation. *Mechatronics*, 46:32-45. https://doi.org/10.1016/j.mechatronics.2017.06.009

Kim J, Heimgartner R, Lee G, et al., 2018. Autonomous and portable soft exosuit for hip extension assistance with online walking and running detection algorithm. Proc IEEE Int Con on Robotics and Automation, p.5473-5480. https://doi.org/10.1109/ICRA.2018.8460474

Kim J, Lee G, Heimgartner R, et al., 2019. Reducing the metabolic rate of walking and running with a versatile, portable exosuit. *Science*, 365(6454):668-672. https://doi.org/10.1126/science.aav7536

Kuo CH, Yudha AP, Mohapatra SK, 2018. Force sensorless compliance control of a lower-limb exoskeleton robot. *Int J Autom Smart Technol*, 8(1):51-60. https://doi.org/10.5875/ausmt.v8i1.1565

Li S, Yang J, Chen WH, et al., 2011. Generalized extended state observer based control for systems with mismatched uncertainties. *IEEE Trans Ind Electron*, 59(12):4792-4802. https://doi.org/10.1109/TIE.2011.2182011

Long Y, Du ZJ, Wang WD, et al., 2018. Physical human-robot interaction estimation based control scheme for a hydraulically actuated exoskeleton designed for power amplification. *Front Inform Technol Electron Eng*, 19(9):1076-1085. https://doi.org/10.1631/FITEE.1601667

Luenberger D, 1966. Observers for multivariable systems. *IEEE Trans Autom Contr*, 11(2):190-197. https://doi.org/10.1109/TAC.1966.1098323

Nagarajan U, Aguirre-Ollinger G, Goswami A, 2016. Integral admittance shaping: a unified framework for active exoskeleton control. *Robot Auton Syst*, 75:310-324. https://doi.org/10.1016/j.robot.2015.09.015

Polyakov A, 2011. Nonlinear feedback design for fixed-time stabilization of linear control systems. *IEEE Trans Autom Contr*, 57(8):2106-2110. https://doi.org/10.1109/TAC.2011.2179869

Seo K, Kim K, Park YJ, et al., 2018. Adaptive oscillator-based control for active lower-limb exoskeleton and its metabolic impact. Proc IEEE Int Conf on Robotics and Automation, p.6752-6758. https://doi.org/10.1109/ICRA.2018.8460841

Shtessel Y, Edwards C, Fridman L, et al., 2014. Sliding Mode Control and Observation. Springer, Berlin, Germany. https://doi.org/10.1007/978-0-8176-4893-0

Tan CP, Yu X, Man Z, 2010. Terminal sliding mode observers for a class of nonlinear systems. *Automatica*, 46(8):1401-1404. https://doi.org/10.1016/j.automatica.2010.05.010

Tanghe K, Aertbeliën E, Vantilt J, et al., 2018. Realtime delayless estimation of derivatives of noisy sensor signals for quasi-cyclic motions with application to joint acceleration estimation on an exoskeleton. *IEEE Robot Autom Lett*, 3(3):1647-1654. https://doi.org/10.1109/LRA.2018.2801473

Wang ZW, Liang B, Wang XQ, 2018. Chattering-free fixed-time control for bilateral teleoperation system with jittering time delays and state constraints. *IFAC*, 51(32):588-593. https://doi.org/10.1016/j.ifacol.2018.11.487

Wang ZW, Chen Z, Zhang YM, et al., 2019a. Adaptive finite-time control for bilateral teleoperation systems with jittering time delays. *Int J Robust Nonl Contr*, 29(4):1007-1030. https://doi.org/10.1002/rnc.4423

Wang ZW, Chen Z, Liang B, 2019b. Fixed-time velocity reconstruction scheme for space teleoperation systems: exp barrier Lyapunov function approach. *Acta Astron*, 157:92-101. https://doi.org/10.1016/j.actaastro.2018.12.018

Xiao B, Yin S, 2016. Velocity-free fault-tolerant and uncertainty attenuation control for a class of nonlinear systems. *IEEE Trans Ind Electr*, 63(7):4400-4411. https://doi.org/10.1109/TIE.2016.2532284

Xue T, Wang Z, Zhang T, et al., 2018. The control system for flexible hip assistive exoskeleton. Proc IEEE Int Conf on Robotics and Biomimetics, p.697-702. https://doi.org/10.1109/ROBIO.2018.8665203

Xue T, Wang Z, Zhang T, et al., 2019. Adaptive oscillator-based robust control for flexible hip assistive exoskeleton. *IEEE Robot Autom Lett*, 4(4):3318-3323. https://doi.org/10.1109/LRA.2019.2926678

Yang Y, Hua CC, Li JP, et al., 2017. Finite-time output-feedback synchronization control for bilateral teleoperation system via neural networks. *Inform Sci*, 406:216-233. https://doi.org/10.1016/j.ins.2017.04.034

Yang ZY, Gu WJ, Zhang J, et al., 2017. Force Control Theory and Method of Human Load Carrying Exoskeleton Suit. Springer, Berlin, Germany. https://doi.org/10.1007/978-3-662-54144-9

Zhang T, Tran M, Huang H, 2019. Admittance shaping-based assistive control of SEA-driven robotic hip exoskeleton. *IEEE/ASME Trans Mech*, 24(4):1508-1519. https://doi.org/10.1109/TMECH.2019.2916546

Zhu Z, Xia Y, Fu M, 2011. Attitude stabilization of rigid spacecraft with finite-time convergence. *Int J Robust Nonl Contr*, 21(6):686-702. https://doi.org/10.1002/rnc.1624

Zoss AB, Kazerooni H, Chu A, 2006. Biomechanical design of the Berkeley lower extremity exoskeleton (BLEEX). *IEEE/ASME Trans Mech*, 11(2):128-138. https://doi.org/10.1109/TMECH.2006.871087